The Pennsylvania State University

The Graduate School

Department of Physics

PRESSURE TUNING

OF PNICOGEN CHALCOGENIDE

THERMOELECTRICS

A Thesis in

Physics

by

Thomas J. Scheidemantel

Submitted in Partial Fulfillment
of the Requirements
for the Degree of

Doctor of Philosophy

August 2004

The thesis of Thomas J. Scheidemantel has been reviewed and approved*
by the following:

John V. Badding
Associate Professor of Chemistry
Thesis Co-Adviser
Co-Chair of Committee

Gerald D. Mahan
Distinguished Professor of Physics
Thesis Co-Adviser
Co-Chair of Committee

Peter E. Schiffer
Professor of Physics

Jorge O. Sofo
Associate Professor of Physics

James B. Anderson
Evan Pugh Professor of Chemistry

Jayanth R. Banavar
Professor of Physics
Head of the Department of Physics

*Signatures are on file in the Graduate School.

Abstract

The thought of a cooling device or power generator with no moving parts seems almost a part of science fiction. Such devices do exist. They are used in a small niche of applications ranging from the cooling of individual solid state components to generating power aboard deep space telescopes. In this document, we present research that attempts to further improve and understand presently used and potentially new thermoelectric materials.

To accomplish this we will use the well established technique of pressure tuning, along with first-principles calculations to study the effects of arsenic on currently used room temperature thermoelectric materials. The small size of arsenic may provide extra degrees of freedom in these currently used alloys.

We found that pressure provides a route to the phase of As_2Te_3 that is isostructural with the rhombohedral ($R\bar{3}m$) structures of Bi_2Te_3 and Sb_2Te_3. The ambient pressure phase of As_2Te_3 is monoclinic. We also found that As_2Te_3 is more soluble in group V-VI alloys containing Sb_2Se_3 than in Bi_2Te_3 or Sb_2Te_3 alone.

We also present a new host for low-dimensional thermoelectric structures. Some thermoelectric properties are enhanced by lowering the dimensionality of some materials. Current research though uses hosts and techniques that are expensive and not feasible for scaling up to commercial levels. We present a host and some techniques that may make this up-scaling a reality.

Table of Contents

List of Tables

List of Figures

Acknowledgments

I would like to thank my adviser, John V. Badding, for his leadership and patience throughout my term as a student. I would also like to thank Jorge O. Sofo for his guidance while Professor Badding traveled overseas to conduct research on sabbatical leave. Most of the reasearch contained in this document could not have been completed without co-workers and collaborators - Jin Feng Meng who helped me with thermoelectric power measurements in the diamond anvil cell, Michael McGuire in Professor Francis DiSalvo's group at Cornell University who supplied me with many of the alloys that we studied, and Bryan Robert Jackson who was always available to help with the experiments. I would also like to thank my committee for taking time out of their busy schedules.

Finally, I would not be here without the support of my parents, Thomas G. and Margaret (Peggy) A. Scheidemantel, and my sister Beth A. Scheidemantel, and I thank my wife Sarah E. (Weber) Scheidemantel, and my children Claire J. and George H. Scheidemantel. I am grateful for their patience, assistance, and understanding during the preparation of this thesis.

Chapter 1

Introduction

Thermoelectric devices offer an alternative to conventional compressor based refrigeration systems. They have no moving parts, making them extremely reliable. Their inferior efficiency though, has limited their use to niche applications such as individual solid state component cooling, and portable coolers that plug into vehicle lighters. Thermoelectric devices can also be used as power generators. Again, inferior efficiency limits their use to applications where reliability is more important than performance. Improving the efficiencies of such devices has been the goal of much recent research. That is also the goal of this thesis.

1.1 History

In the nineteenth century, over a span of three decades, three thermoelectric effects were discovered. First, in 1821, Thomas Seebeck noticed that if a loop made from two different metals was heated at one of the junctions, a nearby compass needle was deflected. Now we know that current was flowing, generating a magnetic field, but at that time he tried to correlate the magnetic field directly to the temperature gradient. Next, Jean Peltier, in 1834, found a cooling or heating effect (depending on the direction of current) when a current was passed though a junction of two dissimilar metals. Finally, in 1854, William Thomson demonstrated a third effect and described the relationship

between all three. He showed that when one end of a homogeneous metal bar was heated, a potential difference was generated across the bar.

The effect discovered by William Thomson is now called the Seebeck coefficient, thermoelectric power, or thermopower,

$$S = \frac{\mathcal{E}}{\Delta T} \,,$$
(1.1)

where $\mathcal{E}$ is the potential difference between the two ends of the sample, and ΔT is the temperature difference. The Peltier coefficient, π, defined for a junction of two materials, depends on the amount of heat emitted or absorbed, q, and the current, i,

$$\pi_{ab} = \frac{q}{i} \,.$$
(1.2)

The Thomson coefficient or Thomson heat of a material is the heating or cooling per unit length that is experienced in a given temperature gradient when current is flowing,

$$\mu\frac{dT}{dx}i = \frac{dq}{dx} \,.$$
(1.3)

So, when a current is present, the rate at which heat is dissipated (per unit length) does not depend only on the irreversible Joule heating, but also a Thomson heat term, which depends on the direction of the current flow and the temperature gradient,

$$\dot{Q} = J^2\rho - J\frac{dT}{dx}\mu \,.$$
(1.4)

Thomson found how all of these effects were related, and showed that knowledge of only the Seebeck coefficient is sufficient to determine the other coefficients,

$$\mu = T\frac{dS}{dT} \tag{1.5}$$

$$\pi = TS . \tag{1.6}$$

1.2 Efficiency of Thermoelectric Devices

A thermoelectric cooling device is arranged most similarly to Peltier's experiment (Figure 1.1). Current passing through both legs of the device in series causes the majority carriers to flow away from the heat source. In doing this they carry their thermal energy with them to the heat sink end. A power generator works similarly. Heat applied at the source causes the (thermally) energetic majority carriers to travel down the legs and accumulate at the heat sink end. This imbalance cause a potential difference across the two branches of the device.

The coefficient of performance (COP) for a refrigerator is defined as the the rate at which heat is removed at the heat source divided by the rate at which we do work on the system,

$$\phi = \frac{q_c}{w} . \tag{1.7}$$

The amount of heat removed at the heat source is the heat removed by Peltier cooling working against thermal conduction and Joule heating. The work we must put into the
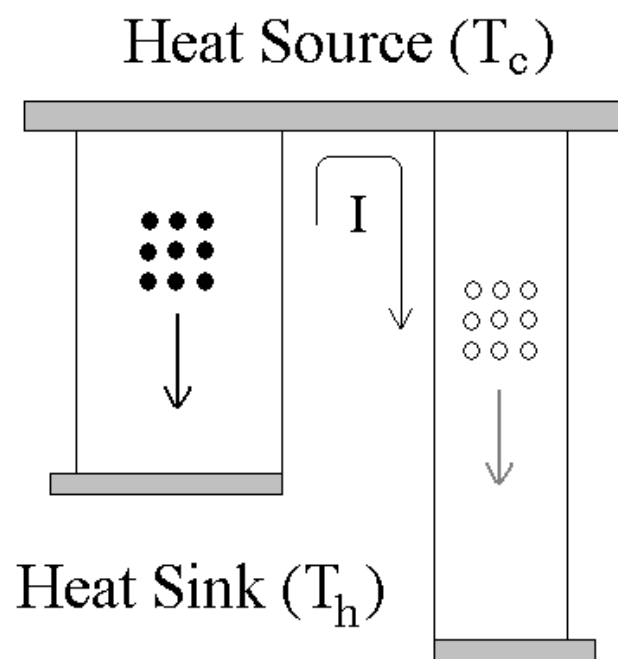
Fig. 1.1. A schematic example of a thermoelectric cooler. The majority carriers of each leg carry their thermal energy away from the heat source in response to the flowing current.

system fuels the Peltier cooling and compensates for Joule heating losses,

$$q_c = iT_c\left(S_p - S_n\right) - \varkappa\left(T_h - T_c\right) - \frac{i^2 R}{2} \tag{1.8}$$

$$w = i\left(T_h - T_c\right)\left(S_p - S_n\right) - i^2 R. \tag{1.9}$$

T_h and T_c are the temperatures of the hot and cold ends. S_p and S_n are the thermopowers of the p and $n-$type branches of the device. R is the resistance of the two branches in series, $\varkappa$ is thermal conductance of the branches in parallel, and i is the current flowing through the device. We can find the optimal COP by maximizing it with respect to the current. We see then that the COP is just the Carnot efficiency, scaled by another fraction,

$$\phi_{opt} = \left(\frac{T_c}{T_h - T_c}\right)\frac{\sqrt{zT+1} - \frac{T_h}{T_c}}{\sqrt{zT+1} + 1} \tag{1.10}$$

where,

$$z = \frac{\left(S_p - S_n\right)^2}{\varkappa R}. \tag{1.11}$$

We can eliminate size effects by optimizing the geometry, after which we are left with the figure of merit for a thermoelectric material,

$$Z = \frac{\sigma S^2}{\kappa}. \tag{1.12}$$

Here the electrical conductivity, σ, and the thermal conductivity, κ, are independent of the size of the sample. We have dropped the subscript labeling the Seebeck coefficient assuming that we have p and $n-$type branches of similar figures of merit.

1.3   Present Efficiencies of Thermoelectric Devices

To date, the best room temperature thermoelectric devices, in commercial production, contain bismuth, antimony, selenium, and tellurium [61, 109]. The pseudo-ternary alloys $(Bi_2Te_3)_{90}$ $(Sb_2Te_3)_5$ $(Sb_2Se_3)_5$ and $(Sb_2Te_3)_{72}$ $(Bi_2Te_3)_{25}$ $(Sb_2Se_3)_3$ have the highest figures of merit at $300K$ for $n-$type and $p-$type materials respectively. SbI_3-doped $(Bi_2Te_3)_{90}$ $(Sb_2Te_3)_5$ $(Sb_2Se_3)_5$ has a figure of merit of 0.96 while the excess Te-doped $(Sb_2Te_3)_{72}$ $(Bi_2Te_3)_{25}$ $(Sb_2Se_3)_3$ has a slightly higher ZT of 1.14 [29, 109].

A single-stage thermoelectric device made from these materials is able to cool a maximum of 78K from room temperature. This represents operating at 7.6% of the maximum Carnot efficiency. A multiple stage device made from such materials achieved a maximum cooling of 159K at room temperature. A good household refrigerator operates at about 30% of its maximum Carnot efficiency and can cool well below freezing. So as far as thermoelectric cooling is concerned, there is room and the need for improvement.

In the laboratory, there has been progress improving thermoelectric efficiency. Experiments on low-dimensional structures have demonstrated that higher ZT's can be attained [24, 26, 39, 102]. Whereas the bulk alloys are easily produced for large scale applications, such quantum wells and nanowires are not. So, in this case we have a large enough figure of merit to compete with conventional refrigeration methods but we do not have the end result device for mass production.

1.4 Current Research

There is currently much research being conducted to find better thermoelectric materials. The known good alloys are being improved [29]. Skutterudites have always been he target for intense research because of their high temperature performance as power generators [100, 106]. Clathrates, having properties of a phonon glass-electron crystal (PGEC), have also been the target of intense research. A PGEC material would have elecronic properties of a good semiconductor, but thermal properties of an amorphous material [88]. Most of the research shown here is purely synthesis based. New materials are synthesized and tested and then more are synthesized and more are tested. Modeling of these structures can help in tuning the materials, but the process can still be very tedious. It can be complimented, though, by pressure tuning which we will discuss later.

There is also much research aimed at the possibility of nanostructures being used as thermoelectric devices. Some efforts use known good bulk thermoelectric materials in superlattices [101, 102]. Some are optimizing quantum well and wire size [38, 40]. Most importantly, some research is aimed at making this technology more useful on a larger scale[74, 107]. This aspect will also be addressed in this thesis.

Looking at equation 1.12, we see that the figure of merit, and hence the efficiency, of a thermoelectric material can be enhanced by lowering the thermal conductivity or raising the electrical conductivity or Seebeck coefficient. One problem is that these three properties are closely related and cannot be tuned completely independent of each other. In this thesis, we attempt to address these problems using old and new techniques.

1.5   Goal of this Thesis

1.5.1   Arsenic

We mentioned earlier that the best bulk alloys are composed of bismuth, antimony, tellurium, and selenium. Groups V and VI of the periodic table (Table 1.1) show what seems to be an obvious trend. Aside from the much lighter elements – nitrogen, oxygen, phosphorous, and sulfur – it seems that arsenic and polonium might complete the picture. We can exclude the hope of using polonium since the naturally occurring isotope has a half-life of only 138.5 days. That leaves arsenic.

Arsenic telluride and arsenic selenide, though, are monoclinic and arsenic selenide has a low melting temperature, eliminating it as a thermoelectric candidate. Bi_2Te_3 and Sb_2Te_3 are rhombohedral with space group $R\overline{3}m$, and Sb_2Se_3 is orthorhombic with space group $Pnma$. Whereas arsenic telluride dissolves only slightly in bismuth or antimony telluride, Sb_2Se_3 forms pseudo-ternary solid solutions over most of the composition range with Bi_2Te_3 and Sb_2Te_3 [95, 108]. It is believed that Sb_2Se_3 is beneficial to the Bi_2Te_3-Sb_2Te_3 system because it widens the energy gap. Sb_2Se_3 has a much larger band gap, $1.11eV$, than bismuth and antimony telluride, $0.16eV$ and $0.25eV$ [6, 54, 86, 78]. The inclusion of Sb_2Se_3 into this system increases the room temperature figure of merit by 21%. A summary of some properties of Group V-VI compounds are shown in table 1.2 [1, 2, 10, 28, 36, 40].

Very little research has been done on crystalline As_2Te_3 and the effect of arsenic on systems such as those shown above. This is due to difficulties in handling arsenic because of toxicity concerns, and difficulties in crystal growth of compounds such as As_2Te_3 and

Table 1.1.   Groups III, IV, V, and VI of the periodic table

13 (III)	14 (IV)	15 (V)	16 (VI)
5 B 10.811	6 C 12.011	7 N 14.00674	8 O 15.9994
13 Al 26.981539	14 Si 28.0855	15 P 30.973762	16 S 32.066
31 Ga 69.723	32 Ge 72.61	33 **As** 74.92160	34 **Se** 78.96
49 In 114.818	50 Sn 118.710	51 **Sb** 121.760	52 **Te** 127.60
81 Tl 204.3833	82 Pb 207.2	83 **Bi** 208.98038	84 **Po** [208.9824]

Table 1.2.
Summary of group V-VI compounds

Compound	Structure	Space Group	Vol. (Å^3)	S $\left(\frac{\mu V}{K}\right)$	ZT
As_2Se_3	Monoclinic	$C2/m$	127.4		0.02(a)
As_2Te_3	Monoclinic	$C2/m$	141.2	245	0.16
Sb_2Se_3	Orthorhombic	$Pnma$	134.6	1200	0.03
Sb_2Se_2Te	Rhombohedral	$R\bar{3}m$	144.0		
Sb_2Te_2Se	Rhombohedral	$R\bar{3}m$	151.6		
Sb_2Te_3	Rhombohedral	$R\bar{3}m$	158.2	80	0.12
Bi_2Se_3	Rhombohedral	$R\bar{3}m$	142.4		
Bi_2Te_2Se	Rhombohedral	$R\bar{3}m$	157.9		
Bi_2Te_3	Rhombohedral	$R\bar{3}m$	169.1	180	0.68

As_2Se_3. Even when mechanically stable crystals are successfully produced, there have been complications experienced in measuring transport properties. Measurements are usually very unstable. Some thermoelectric power measurements have shown $p-$type and $n-$type As_2Te_3 within the same ingot [10].

Here, we will attempt to determine, more completely, the effect of arsenic and arsenic telluride on room temperature thermoelectric cooling. First we discuss the methods we will be using to investigate the compounds being studied. Two methods have been employed. The first is pressure tuning.

Pressure tuning provides a means to change the structure of compounds being studied without having to synthesize a completely new compound. If an improved property is discovered, only then must an attempt be made to synthesize a compound with the same properties at ambient pressure. Pressure tuning is discussed in Chapter 2.

The second method we use to search for improved thermoelectric materials begins with first-principles calculations. In Chapter 3 we discuss the derivation of transport coefficients from band structures calculated using the full potential linearized augmented plane wave method (FP-LAPW) within density functional theory.

First we will look at the band structure of As_2Te_3 and how it may compare to Bi_2Te_3 in Chapter 4. We will look at two known phases of arsenic telluride, the monoclinic $\alpha-$phase discussed earlier, and the high pressure $\beta-$phase which is isostructural with Bi_2Te_3 and Sb_2Te_3. In Chapter 5 we will then study transport properties of As_2Te_3 under pressure and study the effect of arsenic in the alloys mentioned earlier in this chapter.

1.5.2 Low-Dimensional Thermoelectrics

In section 1.5.1 we looked at research aimed at bulk thermoelectric materials. In Chapter 6, we will study one of the newest paths in the search for improved thermoelectrics. In the past ten years, the suggestion of lower dimensionality as a way to increase ZT has matured into an intensively studied field of thermoelectrics [23, 24, 26, 27, 57]. Here we will discuss a newly designed deposition method, with a recently designed host. We will demonstrate depositing low-dimensional structures in large scale host materials.

Chapter 2

Experimental Methods
in the Diamond Anvil Cell

2.1 Introduction

Pressure tuning provides a means for varying a compounds volume which can change the electronic structure and bonding properties. This permits a clean optimization of properties without the unwanted effects of chemical tuning such as disorder or phase separation. Traditional synthesis techniques are also slow compared to pressure tuning since the reaction methods, doping levels, and compositions must be varied to synthesize a single target compound. Pressure tuning is possible using a diamond anvil cell (DAC).

There have been recent rapid advances in high pressure technology that allow the measurement of many physical properties inside the DAC. For our purposes, the pressure, thermoelectric power, and resistance can all be measured without having to remove the sample. X-ray powder diffraction patterns and Raman spectra can be acquired for samples in the DAC as well. All of these methods offer a way of tuning a material quickly and simply. If desirable results are obtained, a target is set, and synthesis of a new compound, with the desired structure at ambient pressure, is attempted.

2.2   Sample Preparation

A diagram of a typical Mao-Bell DAC used in our lab is shown in figure 2.1. Figure 2.1a shows a close-up view where the opposing diamonds can be seen. The drilled steel gasket radially contains the sample and pressure medium. Figure 2.1b shows the assembly in the body which acts as a vise to press the two diamonds together, thereby compressing the sample (Figure 2.2).

To prepare a sample, first the stainless steel gasket is drilled and coated with electrically insulating varnish. The varnish is spread around the edge of the drilled hole to prevent the thermocouples from making electrical contact with the conductive gasket. When the varnish dries, monoclinic zirconium powder is placed in the drilled hole and a small amount of cesium iodide is placed in the very center of the hole. The CsI is transparent to visible and IR light in the range of pressures we explore. This allows visualization of the sample while laser heating. Both media are then compacted by the opposing diamond. This "pie crust" is baked at $100^{\circ}C$. The sample is then placed on this smooth crust and pressed down into the ZrO_2 and CsI. Next, two $12.5\mu m$ chromel-alumel thermocouples are placed across the sample approximately $400\mu m$ apart with the welded joint centered on the long axis of the sample. After the thermocouples are pressed down onto the sample, more CsI and ZrO_2 is placed on top of the sample-thermocouple assembly. This is compressed and baked at $100^{\circ}C$ again. A small piece of ruby is placed on top of the sample for pressure measurements to be described later. Insulating varnish and tape are then applied where the thermocouples could make contact with the gasket or opposing diamond seat. The $12.5\mu m$ thermocouples are soldered to heavier gauge

Piston-Cylinder Assembly

(a)

(b)
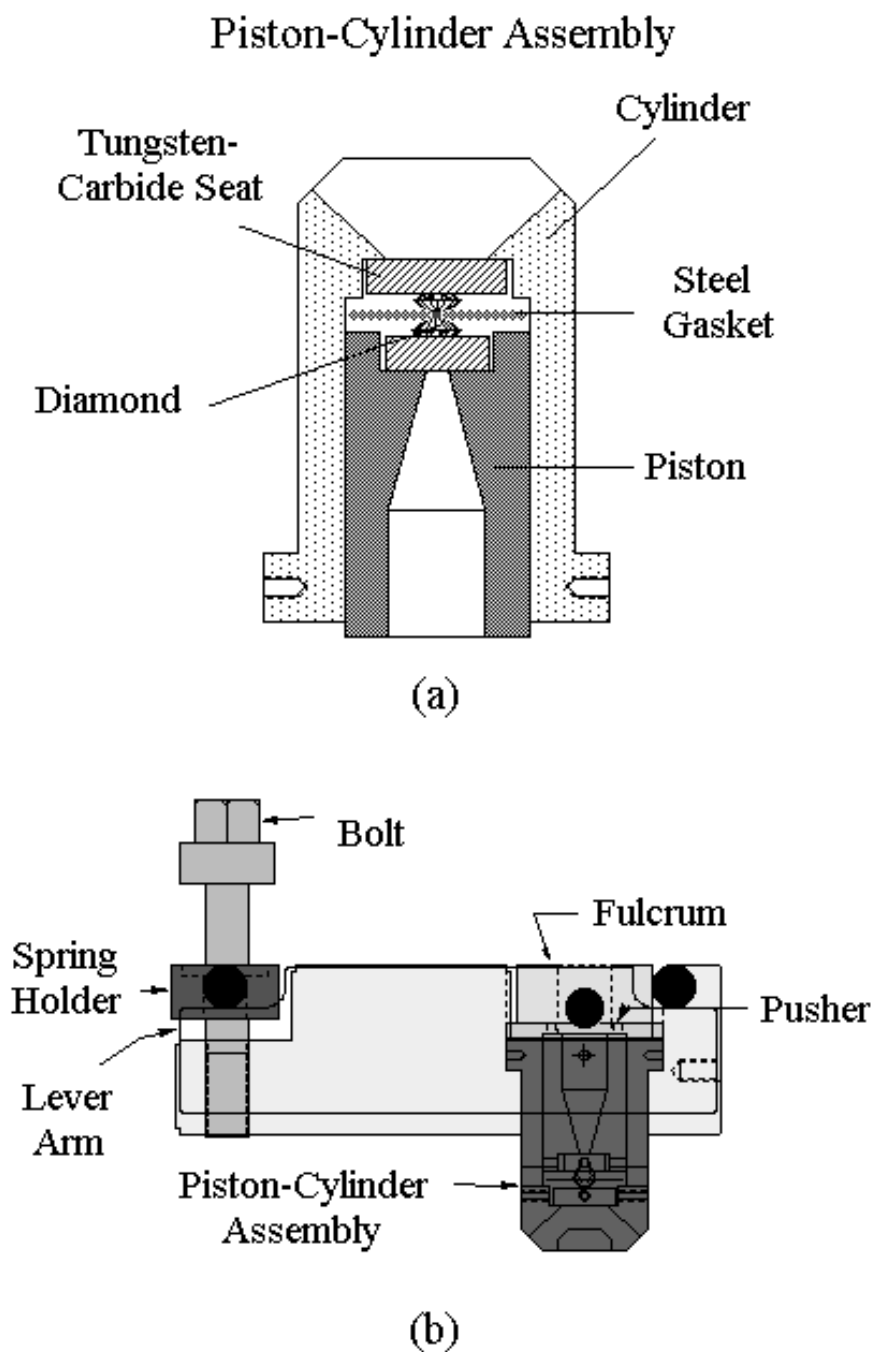
Fig. 2.1. The piston-cylinder assembly (a) of the Mao-Bell diamond anvil cell used in our lab. The assembly is shown in the cell body (b).
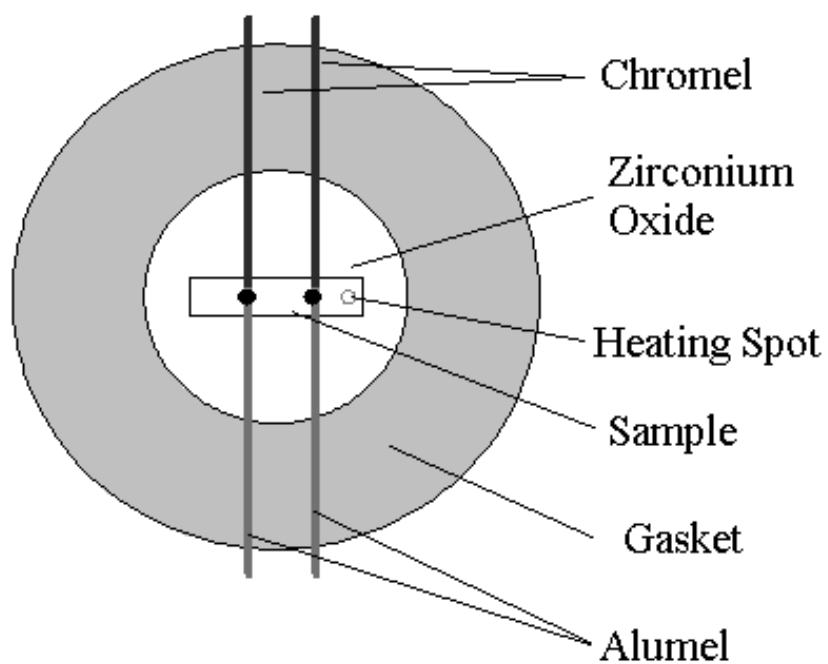
(a)
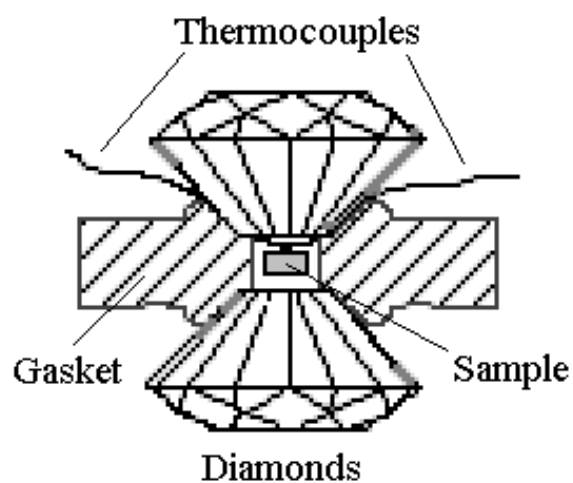
(b)

Fig. 2.2. A view of the sample assembly looking down the axis of the diamond (a) and from the side (b) is shown.

thermocouple extension wire for easier connections outside the DAC. The piston and cylinder are then assembled, and placed in the cell body.

2.3 Measurement of Thermoelectric Power

To measure the thermoelectric power, each of the thermocouple leads must be connected to a digital nanovolt-meter (DVM) [87]. We must compensate for the thermocouples being connected to the copper leads by immersing the thermocouple-copper connections in a $0^{\circ}C$ reference bath. The DAC body is then mounted on a three dimensional stage to allow centering and focusing on the sample inside the cell. The sample can be viewed *in situ* using visible light focused onto a CCD camera. The CCD camera, which is also sensitive to IR radiation, allows focusing the Nd-YAF laser beam onto the sample for laser heating.

The Seebeck coefficient can be defined for a junction of two different materials,

$$S_{12} = \frac{\mathcal{E}_{12}}{\Delta T_{12}} \, , \tag{2.1}$$

or

$$S_s - S_{tc} = \frac{\mathcal{E}_s - \mathcal{E}_{tc}}{T_s - T_{tc}} \, . \tag{2.2}$$

Here the subscript s refers to the sample and tc refers to the thermocouple. If we combine equation (2.2) for the chromel leg of the thermocouple, with equation (2.2) for the alumel leg of the thermocouple we obtain,

$$S_s = \frac{S_a - rS_c}{1 - r} \, , \tag{2.3}$$

where

$$r = \frac{\mathcal{E}_{aa}}{\mathcal{E}_{cc}} \; .$$

(2.4)

$\mathcal{E}_{aa}$ and $\mathcal{E}_{cc}$ are the voltage differences between each of the alumel, and each of the chromel legs of the thermocouples. The thermoelectric powers of the thermocouple materials are well documented ($S_a = -18.39 \mu V/K$ and $S_c = 21.65 \mu V/K$). We can then calculate the thermoelectric power of the sample after measuring the voltage differences across the thermocouple leads.

We do not take the pressure dependence of the thermocouple's thermopower into consideration when we calculate the thermopower of the sample. It has been shown that at 10 GPa, the chromel and alumel alloys do not depart more than $0.6 \mu V/K$ from their ambient pressure thermopowers [15].

Resistance measurements are made using the thermocouples in a psuedo-four probe configuration. A know current is passed through the sample using one set of thermocouple branches, while the voltage drop is measured with the other. The resistance is calculated directly by the DVM.

2.4   Powder X-ray Diffraction and Raman Spectroscopy

If we are interested in results from transport measurements, it is necessary to extract structural information from the sample in the DAC using x-ray diffraction. While Raman spectroscopy can give some information about bonding and structure, powder diffraction can yield precise data from which cell parameters and atomic positions can be determined. By using radiation of constant wavelength incident on a powder sample, we

can use Bragg's Law for constructive interference to calculate the inter-planar spacings in the crystal cell. Bragg's law states [81],

$$\lambda = 2d \sin \Theta \, , \tag{2.5}$$

where λ is the wavelength of the incident radiation, d is the spacing between lattice planes, and Θ is the angle of incidence and reflection.[1]

The x-ray diffraction method used in the DAC was designed in our laboratory [5]. We use a Rigaku Rotaflex RU-200 x-ray diffractometer with a rotating molybdenum ($\lambda = 0.7093$ Å) anode. The x-rays are focused with a Johansson-Gunier curved quartz monochromator and a fabricated collimator (Figure 2.3). The resulting beam is a square with $100\mu m$ sides. The diffracted x-rays are incident on Kodak DEF-128 direct exposure film, which is developed using conventional techniques. The patterns on the film are then scanned into a computer to be interpreted by fitting them to ellipses [69]. The distance between the sample and the film (which affects Θ) is determined from diffraction patterns of standards.

To measure the pressure inside the DAC, the ruby fluorescence method is used [30]. Until the 1970's, compounds that had well known volume equations of state were used as pressure markers in the sample chamber. Pressure estimates made in this manner were unreliable though, because of losses due to friction and gasket flexing. Ruby is much more reliable, not only because the shift in its fluorescence spectrum depends

---

[1]We will not concern ourselves with n ($n\lambda = 2d \sin \Theta$) since it can be absorbed into the miller indices.
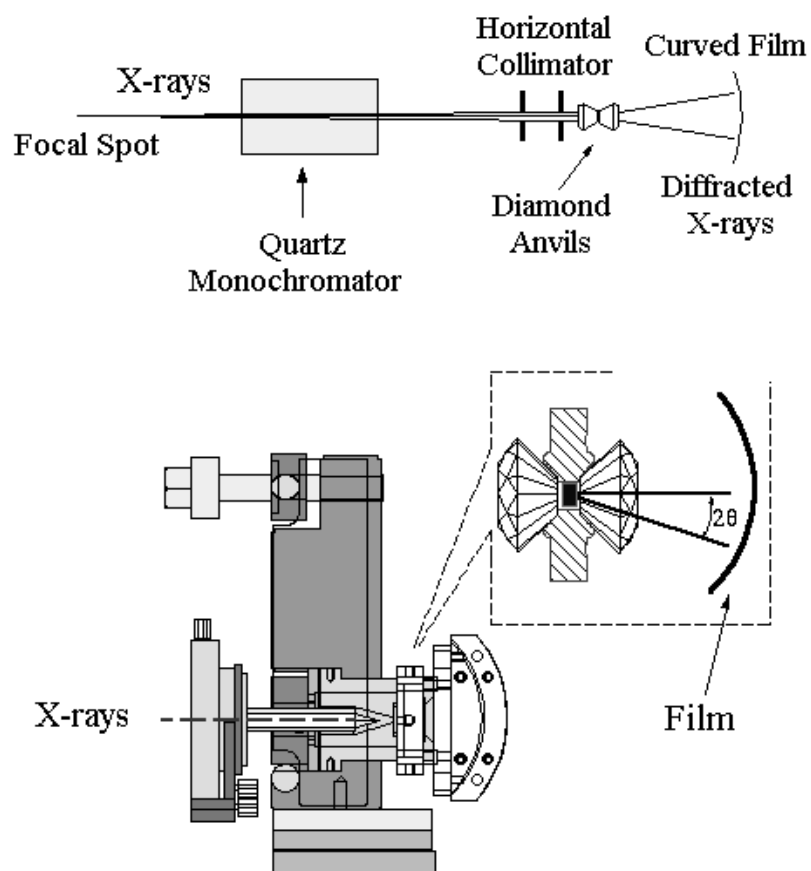
Fig. 2.3.   DAC arrangement for x-ray diffraction experiments.

linearly on pressure, but also because it is chemically inert under increased pressure and temperature. A tiny chip is enough for measurement and practically any visible laser is sufficient. We use a Helium-Neon laser of wavelength $\lambda = 543.5nm$ for our measurements. The ruby fluorescence method has been studied intensely, and the scale has been calibrated precisely up to $100GPa$.

2.5 Results for Standards

As a test for the experimental apparatus, we measured the thermoelectric power of CePd$_3$ up to 10 GPa (Figure 2.4). The thermopower dropped slightly, but stayed between $70\mu V/K$ and $80\mu V/K$. This is in good agreement with previously published results which showed a slight increase in thermopower up to 5 GPa, but it stayed between $76\mu V/K$ and $90\mu V/K$ [72, 92].

Elemental silver was used to calibrate the sample to film distance in the DAC. Silver's interplanar spacings are well documented [93]. The collapsed diffraction pattern is shown in figure 2.5. The d-spacings calculated are in excellent agreement with previously published results if we calculate them using a sample to film distance of $5.0cm$.

2.6 Conclusions

The DAC is a very useful experimental tool. We have shown how the thermopower can be measured while compressing a sample. We have devised a method for x-ray diffraction of samples inside the DAC. The pressure in the sample chamber can be measured accurately with the ruby fluorescence method. These techniques, along with
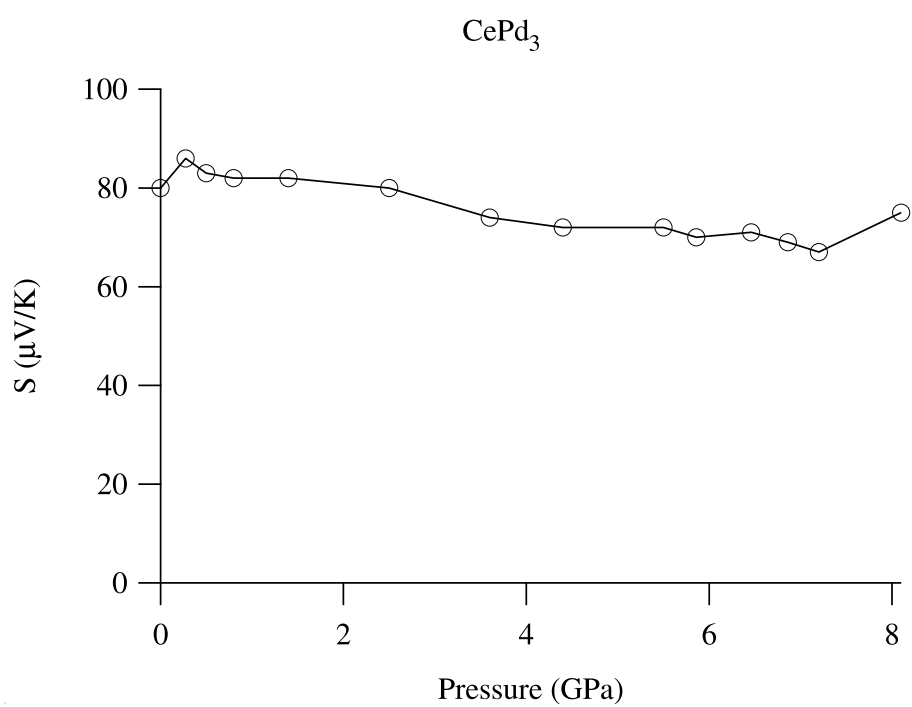
CePd$_3$

Fig. 2.4.   Thermoelectric power of CePd$_3$ versus pressure.
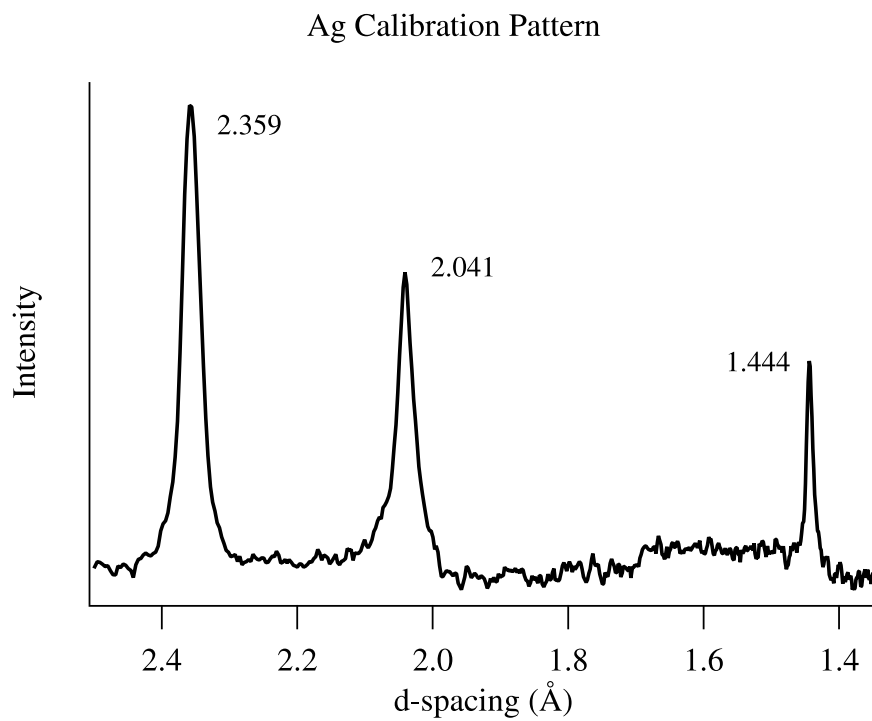
Fig. 2.5. The powder diffraction pattern for silver inside the DAC at zero pressure is plotted versus d-spacing. The distance from the sample to the film is then calculated using the known d-spacing.

the ability to probe the sample structure and bonding nature using Raman scattering,

make the DAC is a very powerful research tool.

Chapter 3

Transport Coefficients from
First-Principles Calculations

3.1 Introduction

Transport coefficients, on which the figure of merit of a material depends (Section 1.2), can be modeled utilizing a combination of parameterized band structures and scattering mechanisms fitted to experimental results. Models to account for the effect of alloy scattering and scattering by acoustic and optical phonons, and ionized and neutral impurities on the charge carriers are fitted to experiment. Once this parameterization and fitting is accomplished, the model can be used to explore the effect of variations in composition, temperature, and doping level. This approach works reasonably well as long as the regions to be explored are not too far from the conditions of the experiment used to fit the model. Several examples can be found in the literature [76, 90, 103]. In view of these requirements, it is most applicable to the fine tuning of well established compounds. It is of very limited applicability for the exploration of novel thermoelectric materials, where the available experimental information is limited.

We introduce a different and complementary approach that attempts to obtain as much information as possible from first-principles calculations [84]. The goal is to reduce the empirical information required to a minimum. First-principles total energy calculations using the linear augmented plane wave (LAPW) method are mature and

can give detailed information about the electronic and structural properties of atoms, molecules, crystalline solids, surfaces, and interfaces [34, 43, 53]. The first step in our approach is to obtain the electronic structure from first-principles calculations, retaining the empirical modeling of the scattering mechanisms. However, many of the parameters needed to model the scattering events can be obtained from first principles calculations. This approach is more general and cannot compete in precision with the *ad-hoc* models for a given material. This approach though, can offer valuable insight when little is known about a material.

3.2 The Transport Distribution and Transport Coefficients

To evaluate the transport coefficients we use the semi-classical approach given by the solution of Boltzmann's equation in the relaxation time approximation [4, 59, 66, 111] Electrical and heat currents are fluxes of charge and energy respectively. The electrical current is defined as

$$\vec{J} = e \sum_{\vec{k}} f_{\vec{k}} \, \vec{v}_{\vec{k}} \, , \tag{3.1}$$

and the heat current as,

$$\vec{J}_Q = \sum_{\vec{k}} f_{\vec{k}} \, \vec{v}_{\vec{k}} \, (\varepsilon_{\vec{k}} - \mu), \tag{3.2}$$

where e is the charge of the carriers. The sums run over all quantum numbers of the system that, in the case of a crystalline solid, are the three components of the crystal momentum $\vec{k}$. $f_{\vec{k}}$ is the population of, and $\vec{v}_{\vec{k}}$ is the group velocity associated with, the quantum state labeled by $\vec{k}$. $\varepsilon_{\vec{k}}$ is the energy of state $\vec{k}$ and μ is the chemical potential.

$\vec{v}_{\vec{k}}$ is defined as the gradient in reciprocal space of the dispersion relation of the electrons in the crystal,

$$\vec{v}_{\vec{k}} = \frac{1}{\hbar} \nabla_{\vec{k}} \varepsilon_{\vec{k}} \, . \tag{3.3}$$

The population of the state $\vec{k}$ is, in our case, the solution of the steady state[1] Boltzmann's equation,

$$\left(\frac{\partial f_{\vec{k}}}{\partial t} \right)_{\text{coll.}} + \left(\frac{\partial f_{\vec{k}}}{\partial t} \right)_{\text{fields}} + \left(\frac{\partial f_{\vec{k}}}{\partial t} \right)_{\text{diff.}} = 0. \tag{3.4}$$

This equation states that the rate of change of $f_{\vec{k}}$ due to collisions, external fields, and diffusion is zero, or

$$\left(\frac{\partial f_{\vec{k}}}{\partial t} \right)_{\text{coll.}} = \left(\frac{\partial \vec{k}}{\partial t} \cdot \nabla_{\vec{k}} f_{\vec{k}} \right) + \left(\vec{v}_{\vec{k}} \cdot \nabla_{\vec{r}} f_{\vec{k}} \right) . \tag{3.5}$$

External fields change the carrier momentum at a rate,

$$\frac{\partial \vec{k}}{\partial t} = -\frac{e}{\hbar} \left(\vec{E} + \frac{1}{c} \vec{v}_{\vec{k}} \times \vec{H} \right) , \tag{3.6}$$

and the scattering term, with the inclusion of a relaxation time τ, can be written as,

$$\left(\frac{\partial f_{\vec{k}}}{\partial t} \right)_{\text{coll.}} = -\frac{f_{\vec{k}} - f_{\vec{k}}^0}{\tau_k} \, . \tag{3.7}$$

---

[1]We are interested in the solution of the steady state Boltzmann equation because we are concerning ourselves with only low field DC currents.

Here, f^0 is the equilibrium distribution function.[2] By choice we drop the dependence on the magnetic field. We also ignore the effects due to the size, and shape of the crystal. Assuming that the occupations depart only slightly from equilibrium, we are left with,

$$\frac{f_{\vec{k}} - f_{\vec{k}}^0}{\tau_k} = \frac{e}{\hbar}\ \vec{E} \cdot \nabla_{\vec{k}} f_{\vec{k}}^0 + \left(\vec{v}_{\vec{k}} \cdot \nabla_{\vec{r}} f_{\vec{k}}^0 \right). \tag{3.8}$$

Finally, if we assume that the spatial dependence of $f_{\vec{k}}^0$ is only through the temperature gradient,

$$f_{\vec{k}} = \tau_k\ \vec{v}_{\vec{k}}\ \left(-\frac{\partial f^0}{\partial \varepsilon_{\vec{k}}} \right) \cdot \left(e\ \vec{E} + \frac{1}{T}\ (\varepsilon_{\vec{k}} - \mu)(\nabla\ T) \right) + f_{\vec{k}}^0. \tag{3.9}$$

Inserting the solution into equations (3.1) and (3.2) we obtain,

$$\vec{J}_e = \sigma\ \vec{E} - \aleph \nabla T$$

$$\vec{J}_Q = T\aleph\vec{E} - \kappa_0 \nabla T. \tag{3.10}$$

---

[2]In this case f^0 is the Fermi-Dirac distribution function,

$$f_0 = \frac{1}{e^{(\varepsilon_{\vec{k}} - \mu)/kT + 1}}.$$

Where σ (the electrical conductivity), S (the Seebeck coefficient), and κ_0 (a component of the electronic thermal conductivity) are the transport coefficients defined as,

$$\sigma = e^2 \int d\varepsilon \left(-\frac{\partial f_0}{\partial \varepsilon} \right) \Xi(\varepsilon) \tag{3.11}$$

$$S = \frac{e}{T\sigma} \int d\varepsilon \left(-\frac{\partial f_0}{\partial \varepsilon} \right) \Xi(\varepsilon) \, (\varepsilon - \mu) \tag{3.12}$$

$$\kappa_0 = \frac{1}{T} \int d\varepsilon \left(-\frac{\partial f_0}{\partial \varepsilon} \right) \Xi(\varepsilon) \, (\varepsilon - \mu)^2 \,. \tag{3.13}$$

κ_0 contributes to the electronic thermal conductivity according to,

$$\kappa = \kappa_0 - T\sigma S^2 \,. \tag{3.14}$$

All material dependent information in the transport coefficients, is contained, by definition, in the transport distribution (TD),

$$\Xi = \sum_{\vec{k}} \vec{v}_{\vec{k}} \, \vec{v}_{\vec{k}} \, \tau_{\vec{k}} \,. \tag{3.15}$$

The TD is important in that it simplifies the numerical calculation as well as holds valuable information that, in itself, reveals details about the material being examined. One example of this is anisotropy, something that is not available from the density of states, but can be seen in the TD without actually calculating any transport properties.

3.3 Implementation

To calculate the TD (Equation (3.15)) the group velocities, the energies, and the relaxation times are needed for each $\vec{k}$–point. In this first implementation we take the group velocity from the first-principles calculations but estimate the relaxation time. Direct calculation of the group velocity using the definition given in equation (3.3) is numerically difficult to implement. Electronic structure codes usually evaluate the band energies in a numerical mesh for the Brillouin zone sampling; therefore, the group velocity must be evaluated as a numerical derivative. This differentiation requires the use of a computationally costly, very fine grid. One method currently being implemented to reduce the computational cost employs a Fourier expansion of energy bands. The Fourier expansion can then be analytically differentiated to obtain the group velocity [60]. However, even if the computational cost can be reduced, real materials usually have several bands crossing the Fermi level and each other which poses a difficulty for this strategy.

We use the following approach. The group velocity is related to the momentum,[3]

$$\vec{v}_{n,\vec{k}} = \frac{1}{m}\,\vec{p}_{n,\vec{k}} = \frac{1}{m}\left\langle \psi_{n,\vec{k}} \left| \vec{\hat{p}} \right| \psi_{n,\vec{k}} \right\rangle , \qquad (3.16)$$

if the coefficients are evaluated at zero field. The last part of equation (3.16) is the intra-band optical matrix element. These matrix elements are available in the optical properties package of the FP-LAPW WIEN2k code [3, 11]. We have implemented the calculation of transport coefficients described here as one of the modules of this package.

---

[3]The band index n has been omitted up to this point in order to make the expressions simpler. To recover the full expressions it is sufficient to replace $\vec{k}$ by $(n,\vec{k})$ in all the indices.

Having the optical matrix elements and the electronic band structure, all that remains, in order to calculate the TD, is the relaxation time.

In this first implementation of the transport code, we restrict the scattering mechanisms to those most relevant for compound semiconductors: scattering by acoustic phonons (deformation potential and piezoelectric), non-polar optic phonons, ionized and neutral impurity atoms and alloy scattering [66]. The parameters entering the expressions for the scattering, such as the deformation potential constant, piezoelectric constant, sound velocity, density, optical phonon frequency, and others are presently taken from experiment.

All semiconductors used as thermoelectric materials are doped to optimize the figure of merit. First-principles calculations, however, are performed for stoichiometric compounds. To treat doping we have to resort to approximations. We have chosen to use the simplest approach, the rigid band approximation. We will assume that the band structure remains unchanged as we move the Fermi level to simulate doping. This approximation is good as long as the doping levels used are not high enough to change the bonding properties of the material. To test this approach, we have calculated the TD and transport coefficients for Bi_2Te_3. Sufficient experimental data has been obtained for Bi_2Te_3 to allow for a rigorous evaluation of the method.

3.4 Application to Bi_2Te_3

3.4.1 Computational Details

The crystal structure of Bi_2Te_3 belongs to the spacegroup $R\overline{3}m$ with atoms stacked along the trigonal axis, Te(1)–Bi–Te(2)–Bi–Te(1). For all calculations we used the experimental rhombohedral cell parameters of $a = 10.48$Å and $\alpha = 24.16°$ [68]. Density functional theory was employed as implemented in the WIEN2k code, utilizing the FP-LAPW method [11]. The generalized gradient approximation as described by Perdew, Burke, and Ernzerhof was used for the exchange and correlation potential [70]. A muffin-tin radius, R_{mt}, of 1.48Å separated the core from the interstitial region on both the Bi and Te atoms. An $R \cdot k_{max}$ value of 10, and G_{max} value of 20 were used corresponding to 950 basis functions in the wave function expansion and $13,259$ stars in the interstitial region respectively. The self-consistent field calculation was converged with 231 $\vec{k}$–points, while the optical matrix elements were calculated for a denser mesh of $11,050$ $\vec{k}$–points in the irreducible wedge of the Brillouin zone. Because of the large spin-orbit (SO) effects in Bi_2Te_3, eigenstates were calculated up to $10.0Ry$ and included in the SO calculation. The sum over $\vec{k}$–points in equation (3.15) was evaluated with the Blöchl integration method [12]. A constant, anisotropic relaxation time (discussed in section 3.4.2.2), and experimentally determined lattice thermal conductivities of 1.5 $\frac{W}{m \cdot K}$ along the basal plane and 0.7 $\frac{W}{m \cdot K}$ along the trigonal axis were used at all doping levels [32]. All integrals were evaluated at a temperature of $300K$.

3.4.2   Results

3.4.2.1   Band Structure

To calculate transport properties, an accurate electronic structure is required. Our calculated band structure along commonly explored high symmetry lines is shown in figure 3.1. We have also included a point labeled Υ, chosen such that the line Υ–Γ passes through the lowest conduction band (LCB) and highest valence band (HVB) edges. We find the band edges in the mirror plane, yielding six LCB and six HVB pockets as a result of three-fold rotational symmetry and inversion symmetry. This has been confirmed by experiment [63, 91]. The calculated band gap, $E_g = 0.11eV$, is in good agreement with experiment [86]. Past reports found the LCB edge along the Γ–Z line using the LMTO-LDA and FP-LAPW (WIEN97) methods [56, 65]. This yields only two carrier pockets due to inversion symmetry.

SO effects are very important in Bi_2Te_3 because its constituent elements are heavy. The second variational method used in our calculation depends on the number of states included in the SO perturbation term. This is controlled by the energy window of states included. When states up to $10.0Ry$ are included, the LCB shows six pockets. In contrast, when the default window is used, $-7.0Ry$ to $1.5Ry$, only two pockets are obtained. We studied the dependence of the energy difference between the LCB states along Γ–Z and Γ–Υ on the upper energy limit of states included in the perturbation, and found that the two states' energies move with respect to each other as the upper limit of the energy window is varied. Figure 3.2 shows the difference between the LCB edge energy that we obtain and energy of the state on the Γ–Z line, $\varepsilon_d = \varepsilon_{\Gamma Z} - \varepsilon_{\Gamma \Upsilon}$,
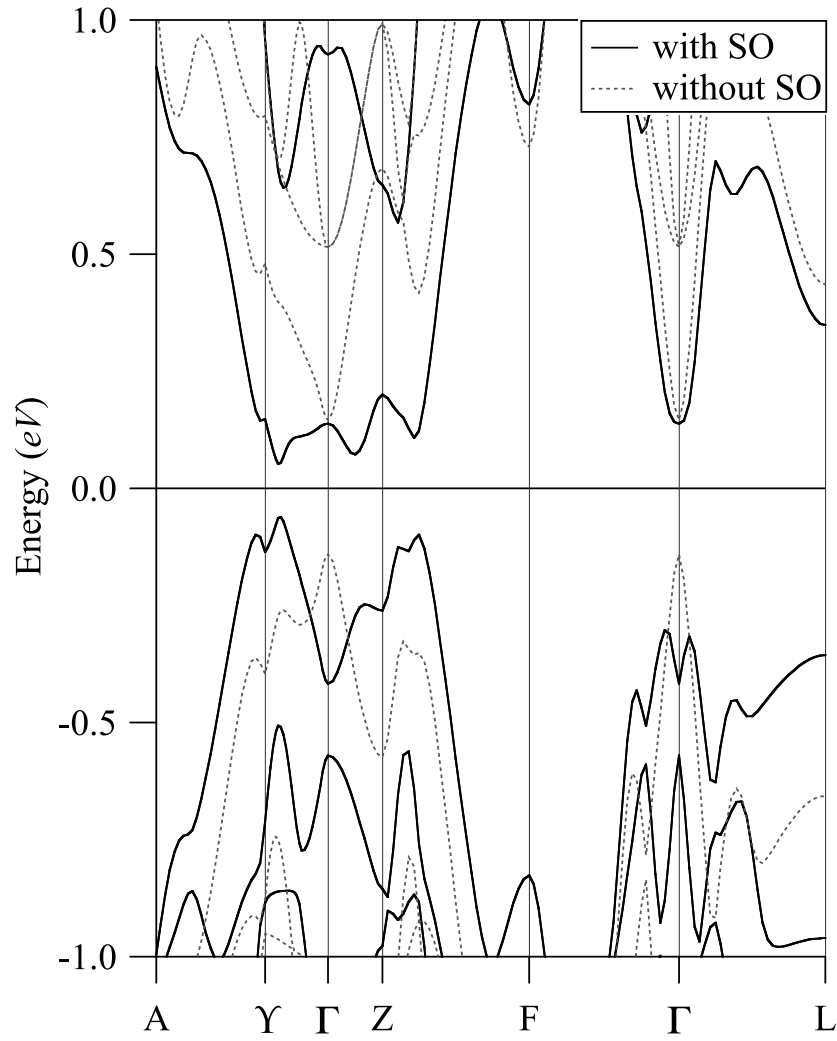
Fig. 3.1. The electronic structure of Bi_2Te_3 is shown with and without SO. The figure shows the importance of SO in Bi_2Te_3 by moving band edges further from the Fermi energy at Γ.

as a function of the upper energy limit. The calculations converge with the Γ–Υ pocket lower in energy, $\varepsilon_d > 0$, leading to six pockets in the LCB. An upper limit of $8.0Ry$ seems to be sufficient. Reference [56] does not mention the energy window used. Other parameters such as R_{mt}, and the number of $\vec{k}$–points used are also different, however these differences do not affect the results. We also compared results between LDA and GGA calculations and found no differences in the location of the band edges.

More recently, Youn et al. found six pockets in both the HVB and LCB using another implementation of the FP-LAPW method and the local density approximation for the exchange and correlation potential [110]. Our LCB edge is the same as, but our HVB edge is slightly different than that found by Youn, et al. We find the HVB edge at $(0.652, 0.579, 0.579)$ (in relative rhombohedral coordinates) and a nearby secondary edge $40meV$ below, at $(0.539, 0.368, 0.368)$, referred to as c and b respectively in figure 3a of Ref [110]. Youn, et al. found the HVB edge at b, and a secondary edge $3.8meV$ lower in energy at c. These differences are small and within the expected precisions of our methods.

With a well converged band structure, and electron velocities calculated as described in section 3.3, we were able to calculate the TD. The integrations were then carried out for different values of the chemical potential to simulate doping as discussed in section 3.3. We first compare our results for the Seebeck coefficient, the electrical conductivity, and ZT with experiment. We then present a general analysis of the TD, power factor (PF), and ZT.
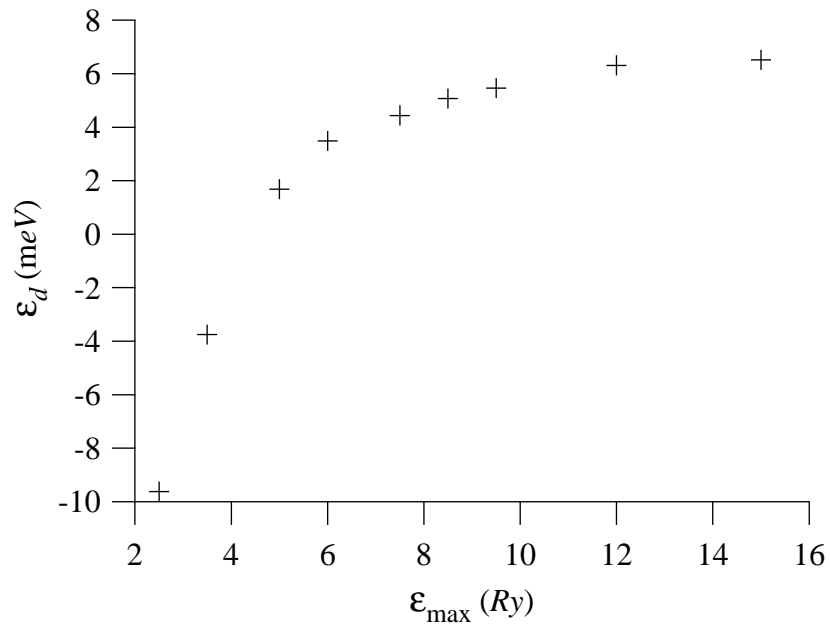
Fig. 3.2. The energy difference between the two states, $\varepsilon_{\Gamma\Upsilon}$ and $\varepsilon_{\Gamma Z}$, is shown versus the upper limit of the energy window used. An upper limit above $8.0 Ry$ is sufficient to produce reliable results.

3.4.2.2 Transport Coefficients of Bi_2Te_3

As is customarily done in thermoelectric literature, we plot S_{xx} (Seebeck coefficient along the basal plane), on the y–axis, and σ_{xx} on the x–axis for samples with different doping concentrations. Figure 3.3 shows experimental data of doped Bi_2Te_3 documented in reference [33] along with our calculated values of the Seebeck coefficient. In calculating the Seebeck coefficient, the constant relaxation time cancels from both integrals (Equations (3.11) and (3.12)) eliminating it as a fitting parameter. We can, however, use τ to fit the Seebeck coefficient with its corresponding electrical conductivity. A constant relaxation time of $\tau_{xx} = 2.2 \times 10^{-14}s$, which gives best agreement in the intrinsic region, was used at all doping levels. We obtain better correspondence on the n-doped side of the graph, but overall, the calculated data agree well with experiment considering that only the relaxation time was adjusted to fit the data.

The anisotropy of the electrical conductivity of Bi_2Te_3 is well documented [67]. The conductivity along the basal plane can be more than four times greater than that along the trigonal axis (zz–direction). This is enough to compensate for a lattice thermal conductivity along the trigonal axis that is half of that along the basal plane. Since the lattice thermal conductivity is comparable to the electronic contribution in the range of reasonable doping, Bi_2Te_3 is used as a thermoelectric device with conduction along the basal plane [33]. Figure 3.4 shows the anisotropy of our calculated electrical conductivity along with experimental data [20]. The data represented by the dotted line were calculated using the relaxation time determined above for conductivity in all directions. The agreement between experimental data and theory is very good. However, if we use
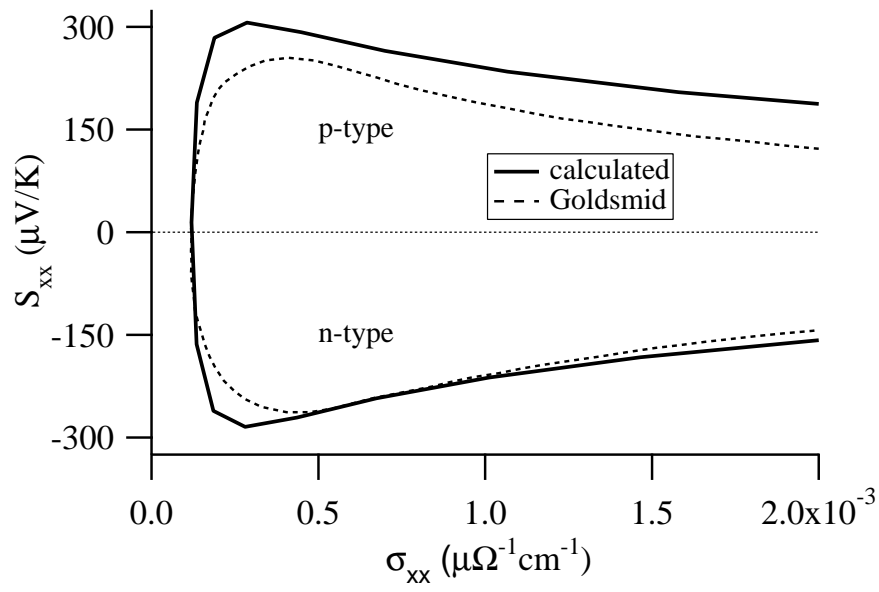
Fig. 3.3.   Calculated Seebeck coefficients with experimental data from reference [33].

an anisotropic relaxation time, $\tau_{xx} = 2.2 \times 10^{-14}s$ and $\tau_{zz} = 2.1 \times 10^{-14}s$, the solid line in figure 3.4 shows even better agreement with experiment. Since this relaxation time is only slightly anisotropic, less than 5% difference between directions, bismuth tellurides's strong anisotropy is a result of its electronic structure, i.e. if any arbitrary, isotropic, constant relaxation time were used, the strong anisotropy of the conductivities would still be apparent. This supports the validity of our calculated band structure. The strong disagreement starting near $\sigma = 4 \times 10^{-3}\Omega^{-1}cm^{-1}$ $(n \gtrsim 10^{20}cm^{-3})$ could be attributed to the failure of the rigid band model at high doping concentrations.

Using the experimentally determined lattice thermal conductivity of intrinsic Bi_2Te_3, we were able to make an estimate of ZT. Figure 3.5 shows experimentally determined figures of merit along with our calculated values [33]. Both sets of data are for ZT calculated along the preferred direction. Again, agreement between calculated values and experiment is quite good. Confident that the band structure and velocities used in the calculations produced reliable results, we now analyze those results to determine which features of bismuth telluride's band structure give rise to a large PF and ZT.

3.4.2.3   Analysis of Transport Coefficients

Figure 3.6 shows several calculated properties plotted as a function of chemical potential (i.e. versus doping in the rigid band model): The TD, DOS, Seebeck coefficient, PF, and ZT. The doping levels represented over the entire range of the plots may be unattainable, but it allows a complete analysis of what gives rise to good electronic properties and ZT. For reference, carrier concentrations up to $10^{20}cm^{-3}$ correspond
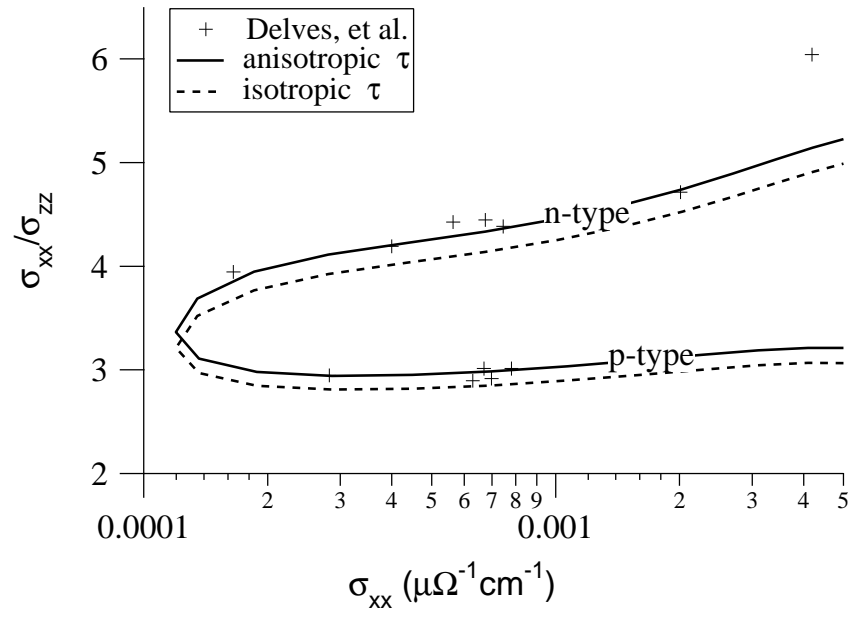
Fig. 3.4.   Calculated electrical conductivity with experimental data from reference [20].
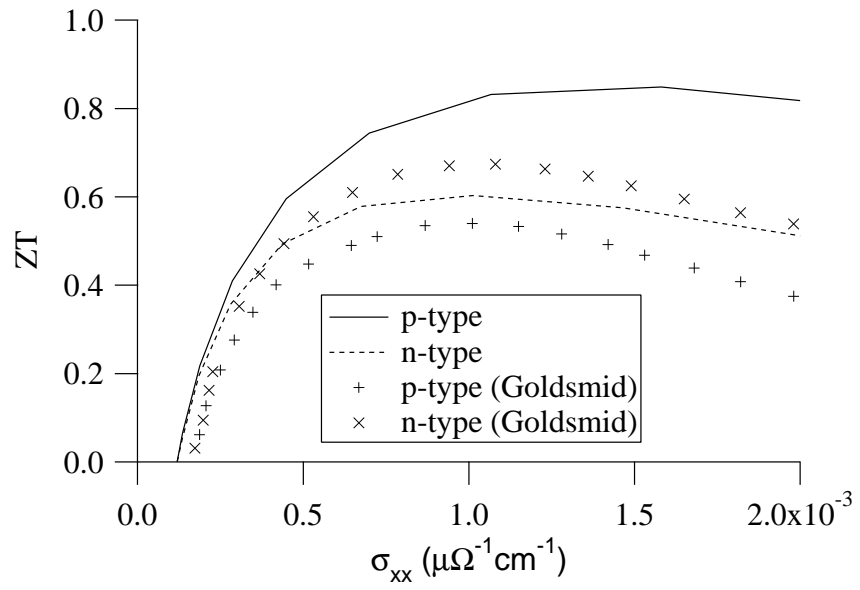
Fig. 3.5.   Estimated values of ZT with data from reference [33].

to chemical potentials between -0.17eV (p-doped) and 0.17eV (n-doped). First we will focus on the PF and Seebeck coefficient because the value of ZT is complicated by contributions from the lattice thermal conductivity.

In figure 3.6, there is no evident correlation between the structure of the TD or DOS and peaks in the PF. Looking at equations (3.11)–(3.13), $\frac{\partial f_0}{\partial \varepsilon}$ dictates the range of the integral. Because $5kT$, the width of $\frac{\partial f_0}{\partial \varepsilon}$, is small compared to the bandwidth, we can approximate the TD as a line,

$$\Xi(\varepsilon) \approx a(\varepsilon - \mu) + b \,, \tag{3.17}$$

where a and b are, respectively, the slope and the height of the TD. Evaluating equations (3.11) and (3.12) using this approximation, it is easy to show that the PF behaves as,

$$\sigma S^2 \propto \frac{a^2}{b} \,. \tag{3.18}$$

The PF grows with increasing slope, or decreasing height of the TD. This is evident near $-0.6eV$ in figure 3.6a, where the two TD's intersect. Here, the xx and zz–directions have equal values of TD, but along the $zz-$direction the slope is larger. Equation (3.18) predicts a larger PF for the TD with the larger slope. Figure 3.6d shows that the PF along the $zz-$direction is indeed greater than that along the xx–direction. This behavior also manifests itself near $0.75eV$ on the n-doped side of figure 3.6a.

The Seebeck coefficient, plotted in figure 3.6c shows more structure in the range of attainable doping levels near the Fermi energy. The approximation of equation (3.17) gives a Seebeck coefficient that behaves as $\frac{a}{b}$. This makes it more sensitive to a larger
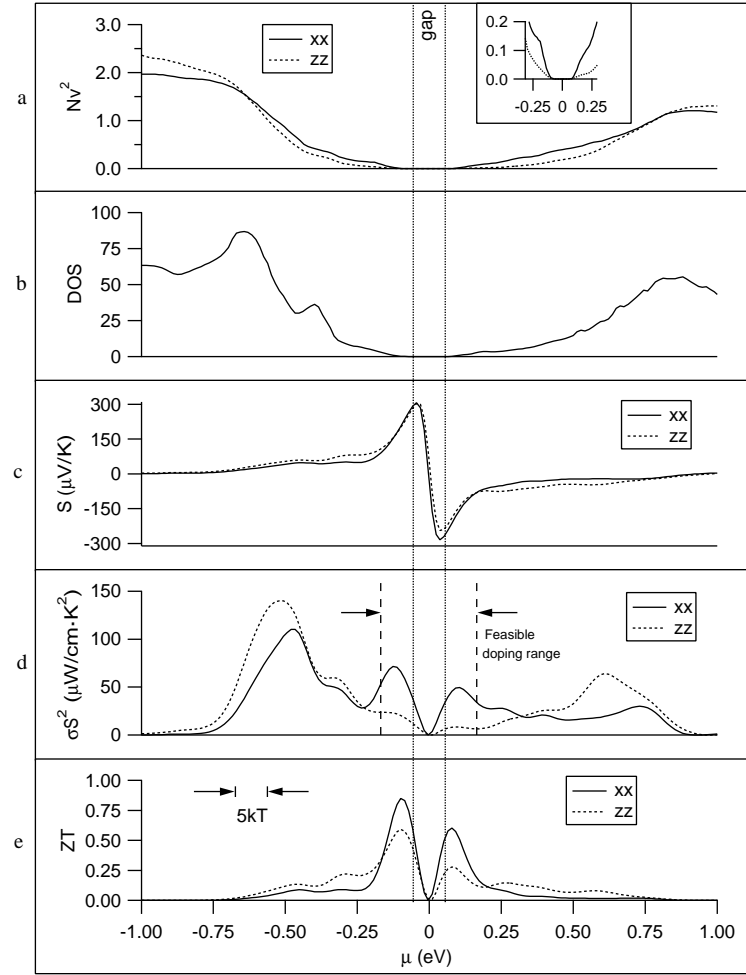
Fig. 3.6. The (a) TD, (b) density of states, (c) Seebeck coefficient, (d) PF, and (e) ZT are all plotted versus chemical potential. Lines depicting the size of Bi_2Te_3's energy gap span the plot. Lines indicating a reasonable doping range ($n, p < 10^{20} cm^{-3}$) are shown with the PF (d).

height of the TD (or larger electrical conductivity). Comparing this to equation (3.18), and by looking at figure 3.6, we see that the optimum Seebeck coefficient does not correspond to the the optimum PF.

All but two of the peaks in the PF lie outside the range of reasonable doping. The benefit of these peaks away from the gap is moot, due to a large κ_{el} that would accompany heavy doping. Figure 3.6e shows ZT's calculated from our data and the experimentally determined lattice thermal conductivity discussed in section 3.4.2.2. One p-type and one n-type maximum, corresponding to $5 \times 10^{19} cm^{-3}$ and $4 \times 10^{19} cm^{-3}$ carrier concentrations respectively, remain at reasonable doping levels. Both agree with experimentally optimized ZT's. The inset of figure 3.6a shows a closer view of the TD that gives rise to these peaks. This shows the importance of the band gap in Bi_2Te_3. Near the gap, b can be very small while a can be large. This does not imply, however, that the gap needs to be small or that this condition only occurs near the gap.

3.5   Conclusions

Starting from basic transport equations we have defined the TD, which is obtainable from first-principles calculations. The TD contains all the electronic information necessary to describe a material. The optical matrix elements needed are already available in the LAPW basis. The method was tested on a material that has been thoroughly investigated (Bi_2Te_3) and the calculated transport coefficients are in agreement with those reported by experiment. The TD was also used to analyze the relationship between the electronic structure of Bi_2Te_3 and its thermoelectric properties. The transport

coefficients can be easily extracted from the slope and value of the transport distribution alone. The power factor is proportional to the square of the slope and inversely proportional its value.

The method presented here should prove valuable in the search for improved thermoelectric materials. Despite the known limitations of first principles calculations in the treatment of alloys and the limitations of the relaxation time approximation, the method gives a rapid and reliable way to efficiently screen potential candidates for thermoelectric materials. Furthermore, insight can be obtained into which features of a material make it exhibit high ZT, such as which bands contribute to the transport process and what crystal structural features are associated with the high ZT. This knowledge opens the way to tailoring the electronic bands to produce more efficient materials. This is the first step toward the ultimate goal of a parameter free evaluation of thermoelectric transport coefficients.

Chapter 4

Electronic Structure and Transport Properties
of α and $\beta-\mathbf{As_2Te_3}$

4.1 Introduction

Bi_2Te_3 and Sb_2Te_3, both of which have a trigonal unit cell with spacegroup $R\bar{3}m$, are very important thermoelectric materials and have been studied intensively. As_2Te_3, though a Group V-VI semiconductor as well, has a different structure and has not been studied nearly as much. The monoclinic unit cell of As_2Te_3, spacegroup $C2/m$, has 5 inequivalent atoms. It is a layered structure with each of the inequivalent arsenic atoms tetrahedrally (As_1 in figure 4.1) or octahedrally (As_2 in figure 4.1) bonded to the surrounding tellurium atoms [16, 19].

Very few band structure calculations were found in the literature for monoclinic As_2Te_3 ($\alpha-As_2Te_3$) [85]. This is due in part to its large unit cell. As_2Te_3 has been more intensively studied in the amorphous form with emphasis placed on its optical properties. Only a tight binding calculation and band structures for amorphous and alloyed As_2Te_3 were found in the literature [14, 47, 58]. There have been experimental studies on the thermoelectric power and other transport properties [36]. Some of those results are listed in Table 1.2.

β-As$_2$Te$_3$ has the same anisotropic trigonal crystal structure (Fig. 4.2a) as Bi$_2$Te$_3$ and Sb$_2$Te$_3$. It can be formed by rapid quenching from high temperatures during synthesis or by compressing monoclinic α-As$_2$Te$_3$ [49, 99]. Relatively little is known about the properties of β-As$_2$Te$_3$. It was recently reported that there is a large improvement in the thermoelectric figure of merit of Sb$_{1.5}$Bi$_{0.5}$Te$_3$ alloys upon pressure-tuning under non-hydrostatic stress [7, 73]. Recent calculations also show an improvement in the power factor of Sb$_2$Te$_3$ under non-hydrostatic pressure [97]. Substitution of smaller atoms into a crystal structure can sometimes be used to effect a chemical pressure that mimics the effects of physical pressure. Arsenic is smaller than bismuth. At ambient pressure however, the thermodynamically stable crystal structure of As$_2$Te$_3$ is monoclinic and less than 1% of the bismuth atoms in Bi$_2$Te$_3$ can be replaced by arsenic by conventional synthesis techniques, and the resulting alloy is a multi-phase semiconductor [108]. At high pressures or temperatures, where β-As$_2$Te$_3$ becomes stable, it might be possible to form solid solutions that could be quenched to ambient conditions [49]. In general, it is difficult to predict whether solid solutions will form from a pair of isotypic semiconductors, but the size difference between As and Bi appear to be small enough to permit substitution. Quenching of liquid As$_2$Te$_3$–Bi$_2$Te$_3$ alloys from high temperature might also form a route to a solid-state alloy.

The electronic structure near the energy gap of a semiconductor determines its thermoelectric properties [21, 61]. Substitution of As for Bi in the Bi$_2$Te$_3$ crystal structure might, like pressure tuning, provide additional degrees of freedom for tuning the thermoelectric properties if the electronic structure of β-As$_2$Te$_3$ is sufficiently different from that of Bi$_2$Te$_3$. Differences might arise because of the slightly smaller size of arsenic
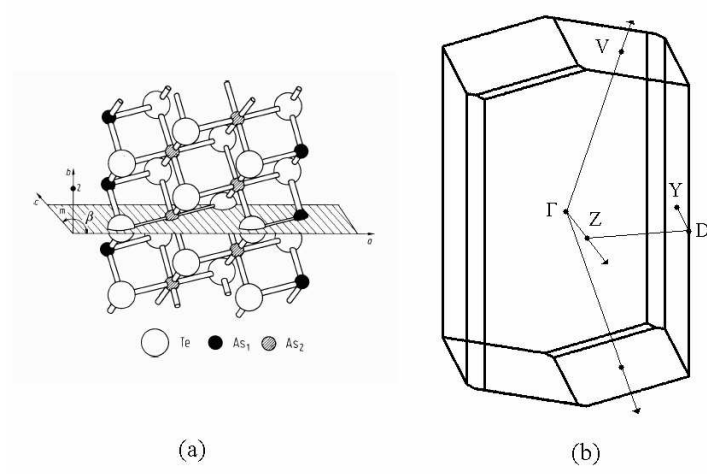
Fig. 4.1.   (a) Layered structure and (b) Brillouin zone of $\alpha-\text{As}_2\text{Te}_3$.
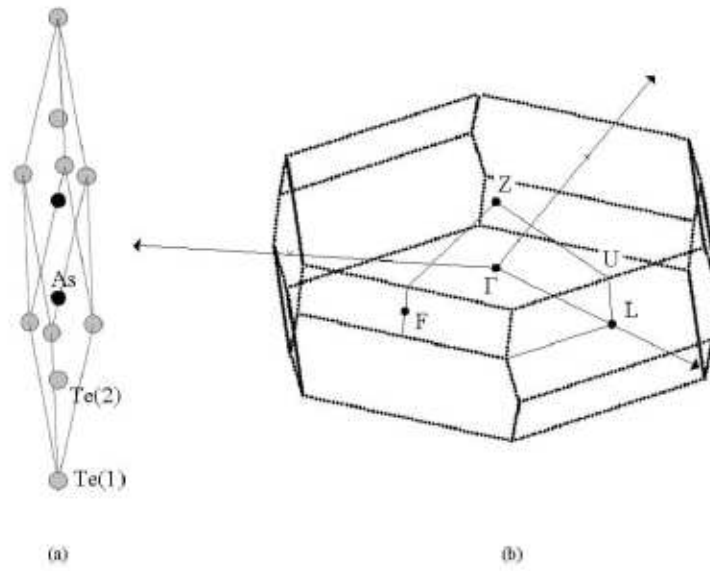
Fig. 4.2.   The (a) rhombohedral β-As_2Te_3 unit cell with the three inequivalent atoms labeled, and (b) the Brillouin zone indicating special $\vec{k}$-points are shown.

and its smaller contribution to the spin orbit interaction relative to bismuth. Here we report a full potential linearized augmented plane wave (FP-LAPW) investigation of the electronic structure of β-As$_2$Te$_3$ using the WIEN2K density functional code [11]. For comparison, we have also calculated the electronic structure of α-As$_2$Te$_3$ and Bi$_2$Te$_3$ using the same method. In contrast to earlier calculations, we optimized the lattice parameters of Bi$_2$Te$_3$ within density functional theory [56, 65, 110]. The electronic structures of β-As$_2$Te$_3$ and Bi$_2$Te$_3$ are similar, although there is a modest difference near the zone center Γ point.

We will also examine transport properties of $\beta-$As$_2$Te$_3$ using the method described in Chapter 3. Again, we expect electronic properties to be similar to that of Bi$_2$Te$_3$. Since arsenic is much lighter than bismuth though, the lattice thermal conductivity may be much higher in β-As$_2$Te$_3$. This would significantly lower ZT.

4.2   Method

The FP-LAPW method was used to solve the Kohn-Sham equations self consistently and the generalized gradient approximation of Perdew, Burke, and Erzenhoff was used to describe the exchange-correlation energy [53, 70]. The muffin-tin radii (R_{mt}) used as the boundaries of the interstitial regions and the ion cores were 1.22Å for arsenic and 1.32Å for tellurium. The core energy cut-off was set at $-6.0Ry$. We calculated the electronic structure using lattice parameters that were relaxed within density functional theory. A mesh containing 344 $\vec{k}$-points in the irreducible wedge of the Brillouin zone (BZ) (Figure 4.2b) was used for convergence. The spin orbit (SO) interaction was included. A G_{max} value of 20.0 and a $R_{mt} \cdot \vec{k}_{max}$ value of 10.0 were used corresponding

to $1,383$ planes waves in the wave function expansion and $14,272$ stars in the interstitial region. After convergence, the BZ was searched for band edges, and once found in the mirror plane containing Γ, U, and A, the eigenvalues of $10,000$ $\vec{k}$-points in the plane were calculated. A similar approach was used for Bi_2Te_3 to ensure that the true extrema, which can be missed if only symmetry lines are explored, are located.

To calculate transport coefficients for $\beta-As_2Te_3$, a much denser grid was used than that for convergence. An irreducible wedge containing $3,894$ $k-$points was used for integration. This represents $42,875$ $k-$points in the entire BZ. A relaxation time of 1×10^{-14} seconds was used to compare the transport distribution (TD) and transport properties qualitatively with Bi_2Te_3.

The experimental lattice parameters, $a = 14.4\mathring{A}$, $b = 4.05\mathring{A}$ $c = 9.92\mathring{A}$, and $\beta = 97.0^{\circ}$, were used for $\alpha-As_2Te_3$. $231\vec{k}-$points in the irreducible wedge of the BZ, representing $1000\vec{k}-$points in the entire BZ were used for convergence. R_{mt} for the arsenic and tellurium atoms was the same as that shown above. All cut-offs used, G_{max}, $R \cdot \vec{k}_{max}$, etc., were the same as that used in the $\beta-As_2Te_3$ calculations. Again, SO corrections were included.

Bi_2Te_3 properties were calculated in the same manner as that in chapter 3, with the exception that the lattice was relaxed for the work in this chapter.

4.3   Results and Discussion

4.3.1   Band Structures

4.3.1.1 $\alpha-\mathbf{As_2Te_3}$

$\alpha-\mathrm{As_2Te_3}$ was found to be an indirect band gap semiconductor with $E_g =$ $0.28eV$. Only two experiments with published energy gaps were found. One calculated from conductivity measurements taken at $500K$ reported $E_g = 0.9eV$ [71]. Another found a gap of $E_g = 1.0eV$ using infrared transmission measurements. It is known now that semiconductor gaps are usually underestimated in the local density approximation. The calculated band structure along some symmetry lines (Figure 4.2a) that include the band edges found is shown in figure 4.3. The SO interaction does little more than close the gap slightly.

The highest valence band (HVB) edge at the $\vec{k}-$point labeled h is near (0, 1/4, 0) at (0.021, 0.278, 0.021). With inversion symmetry and a mirror plane, the HVB edge is four-fold degenerate. A secondary edge located at D in the BZ is $40meV$ below the the HVB edge. The lowest conduction band (LCB) edge is also located at D. A tertiary edge along the $\Gamma - D$ line is only $1meV$ below the pocket at D. Since D is at the zone boundary, the LCB is non-degenerate.

The calculated density of states (Figure 4.4) agrees with both local orbital calculations and x-ray photo-emission spectroscopy measurements [8, 14, 18]. The steep DOS at the HVB is due to the multiple pockets described above.
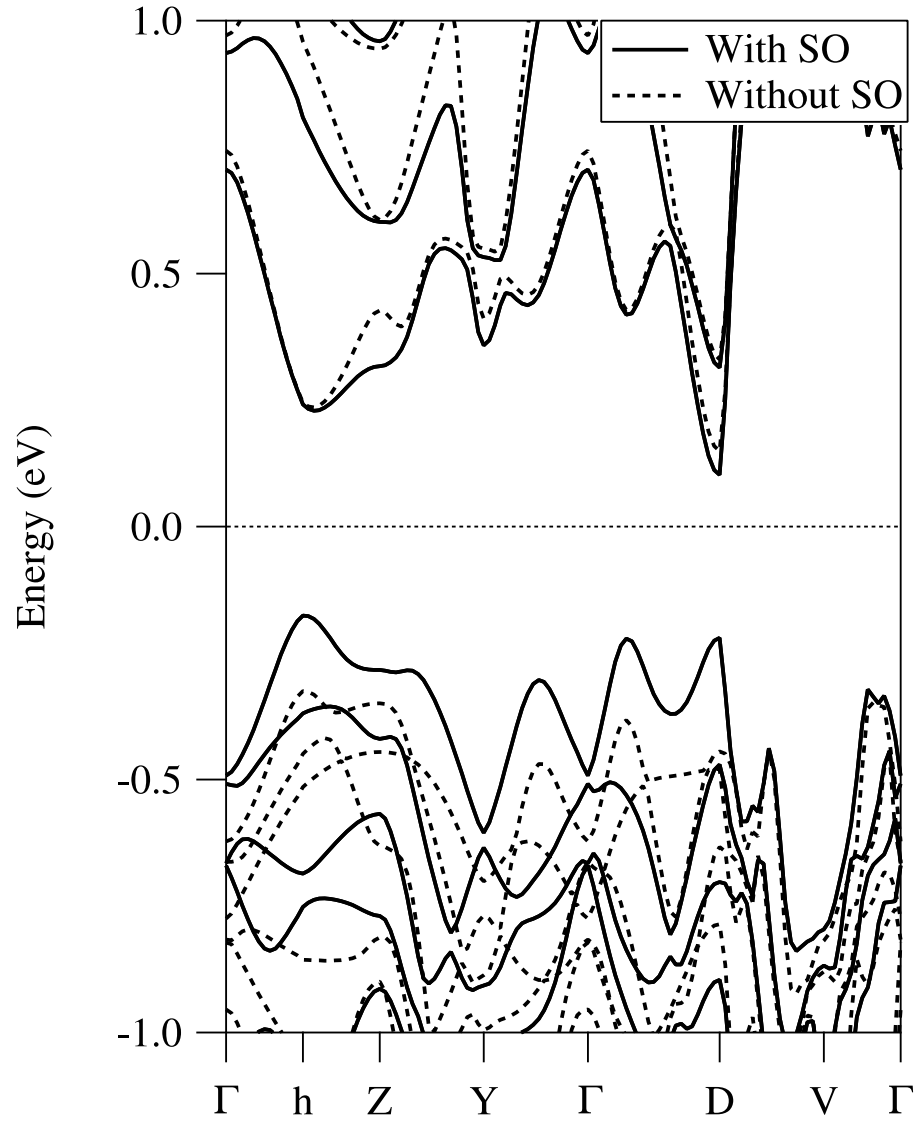
Fig. 4.3. The band structure of $\alpha-\text{As}_2\text{Te}_3$ with and without spin orbit coupling included is shown.
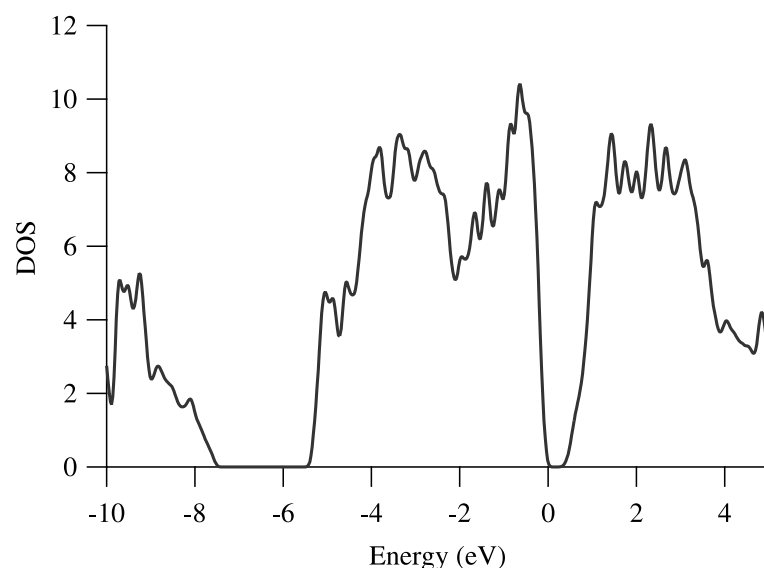
Fig. 4.4. The density of states of $\alpha-\mathrm{As}_2\mathrm{Te}_3$.

4.3.1.2 $\beta-\text{As}_2\text{Te}_3$

The relaxation process for β-As$_2$Te$_3$ yielded a lattice parameter and trigonal angle of $a = 10.27$Å and $\alpha = 23.1^{\text{o}}$ (relaxation of Bi$_2$Te$_3$ resulted in parameters $a = 10.59$Å and $\alpha = 24.4^{\text{o}}$), which differ only slightly from experimental reports [99]. This gives a final relaxed unit cell volume that is 4% larger than the experimental volume. The relaxed atomic positions, which are displaced less than 2% from the experimental positions, are $(0.3951, 0.3951, 0.3951)$ for arsenic and $(0.2183, 0.2183, 0.2183)$ for the second tellurium atom in relative rhombohedral coordinates. The first tellurium atom is fixed at the origin. The bulk modulus derived from a fit of the Murnaghan equation of state to the energy as a function of volume is 50.2 GPa. Although there are no published reports for the bulk modulus of β-As$_2$Te$_3$, the calculated value is in the range observed for most covalently bonded semiconductors, i.e. $B \sim 50 - 100 GPa$.

Contour plots of the energies in the mirror plane containing Γ, U, and Z for both the highest valence band (HVB) and lowest conduction band (LCB) show the location of the band edges in the BZ (Figure 4.5). Both the HVB maximum and LCB minimum lie away from symmetry lines at $\mathbf{m}(-0.316, -0.427, -0.427)$. There are secondary extrema just above the LCB edge and below the HVB edge at Γ. Fig. 4.6 shows the band structure of both β-As$_2$Te$_3$ and Bi$_2$Te$_3$ plotted along lines that include the band edges found for both compounds. We find both of Bi$_2$Te$_3$'s edges located in the mirror plane away from high symmetry lines at the point labeled $\mathbf{b}$ (labeled $\mathbf{d}$ in reference [110]). The secondary LCB edge of β-As$_2$Te$_3$ is within $15 meV$ of the primary edge and will contribute to transport with minimal temperature broadening.
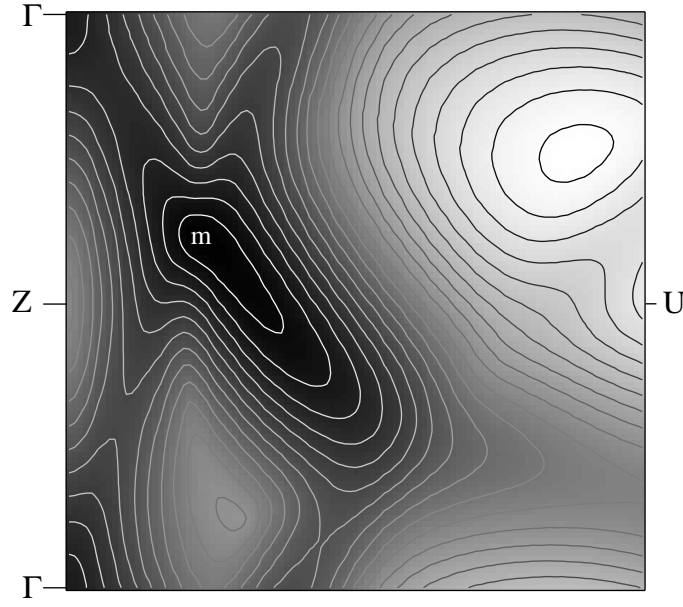
(a)
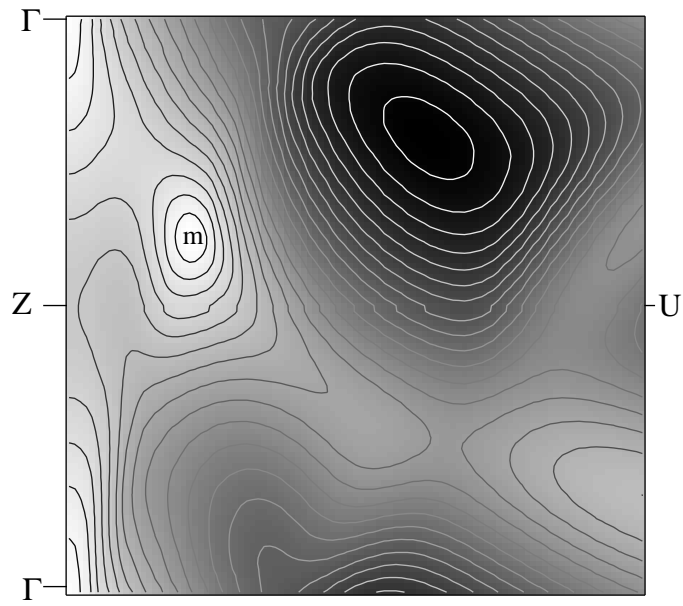
(b)

Fig. 4.5.   Contours of the (a) HVB and (b) LCB in the mirror plane containing Γ, U, and Z are shown. Dark areas indicate maxima and light indicate minima. The band edges are labeled **m**. The contours are separated by $0.1 eV$
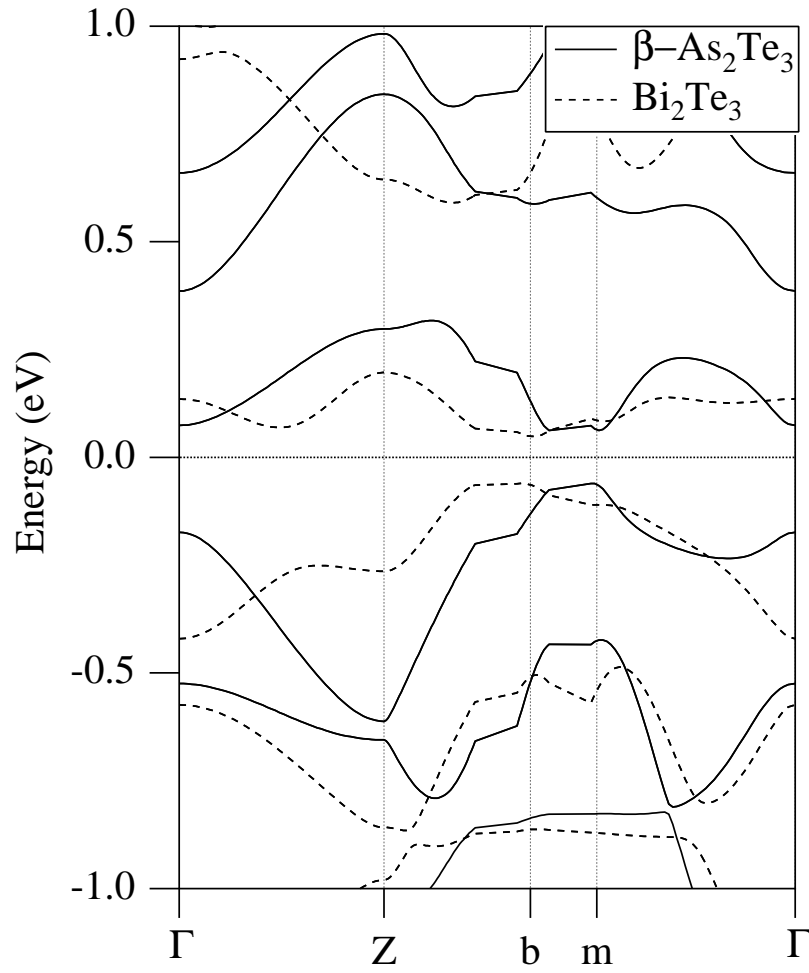
Fig. 4.6. The band structure of β-As$_2$Te$_3$ (solid line) is plotted for comparison with Bi$_2$Te$_3$ (dotted line). β-As$_2$Te$_3$'s band edges are located at **m** and bismuth telluride's at **b**.

Good thermoelectric materials often have multiple valleys at the band edges because higher degeneracies result in higher thermoelectric powers [21, 61]. From rotation and inversion symmetry, the band edges of β-As_2Te_3 at $\mathbf{m}$ must be six-fold degenerate. Models with six valleys in the mirror plane of the Brillouin zone for both the HVB and LCB edges are generally accepted to explain experimental observations of the Fermi surface of doped Bi_2Te_3 [22]. Previous density functional calculations of Bi_2Te_3 that utilized the experimental lattice parameters agree that the valence band has six valleys, but differ on the number of valleys in the conduction band. In agreement with experimental findings, Youn and Freeman found six-fold degeneracy for the conduction band edge [110]. They sampled a large number of $\vec{k}$-points in the Brillouin zone and located the extrema in the mirror plane off of high symmetry lines. Mishra, et al. and Larson, et al. reported a doubly degenerate conduction band valley along the $\Gamma - Z$ direction [56, 65]. The difference between the energies of the band edges found in different calculations is quite small and can be attributed to various differences in the calculation methods employed, such as different approximations for the exchange-correlation potential or different energy cut-offs between core and valence states.

The models proposed to explain the Fermi surface data of Bi_2Te_3 also include a second set of six-fold valleys close in energy to the band edges resulting in twelve Fermi surface pockets at suitable doping levels [63, 91]. The present calculations indicate that, in contrast, the secondary edges of β-As_2Te_3 are at the non-degenerate Γ point (Figures 4.5 and 4.6), while Bi_2Te_3 has local maxima with higher degeneracy on both sides of the Γ point. Γ is also the only point found where the valence band energies are substantially different.

Both the LCB and HVB edges of β-As$_2$Te$_3$ lie at the **m** point in the Brillouin zone giving rise to a direct gap of $\varepsilon_g = 0.12eV$. Youn and Freeman found an indirect gap of $0.061eV$ for Bi$_2$Te$_3$, compared to the experimental gap of $0.13eV$, between the HVB edge at $(0.546, 0.343, 0.343)$ and the LCB edge at $(0.663, 0.568, 0.568)$, labeled **b** and **d** respectively in reference [110], not far from the Z–U line [110]. Larson et al. also reported an indirect gap between the HVB edge at the **a** point along Z–U and the LCB along Γ–Z. The density of states of $\beta-$As$_2$Te$_3$, also very similar to calculated DOS of Bi$_2$Te$_3$, is shown in figure 4.7. The inset shows a closer view of the DOS near the Fermi energy, where it is also very similar to that of Bi$_2$Te$_3$.

4.3.2   Transport Properties

The calculated TD for β-As$_2$Te$_3$ and Bi$_2$Te$_3$ are shown in figure 4.9. The Fermi energies are slightly shifted to expose the structures near the gap. Their behaviors are very similar. The slopes near the gap are quite steep and we would expect the power factor (PF) of β-As$_2$Te$_3$ to be close to that of bismuth telluride. On the valence band side of the TD, Bi$_2$Te$_3$ shows high anisotropy just below the gap. β-As$_2$Te$_3$ though, does not show as much anisotropy until the chemical potential reaches approximately $-0.4eV$. This could indicate a degree of freedom from alloying not apparent from the band structures alone.

Figure 4.9 shows that the PF of $\beta-$As$_2$Te$_3$ does not come close to that of Bi$_2$Te$_3$ near the Fermi energy. For both n and $p-$type compounds, the PF of Bi$_2$Te$_3$ along the $xx-$direction dominates by nearly a factor of four. Since arsenic is smaller than bismuth, it is probable that the thermal conductivity would not be low enough in $\beta-$As$_2$Te$_3$ to
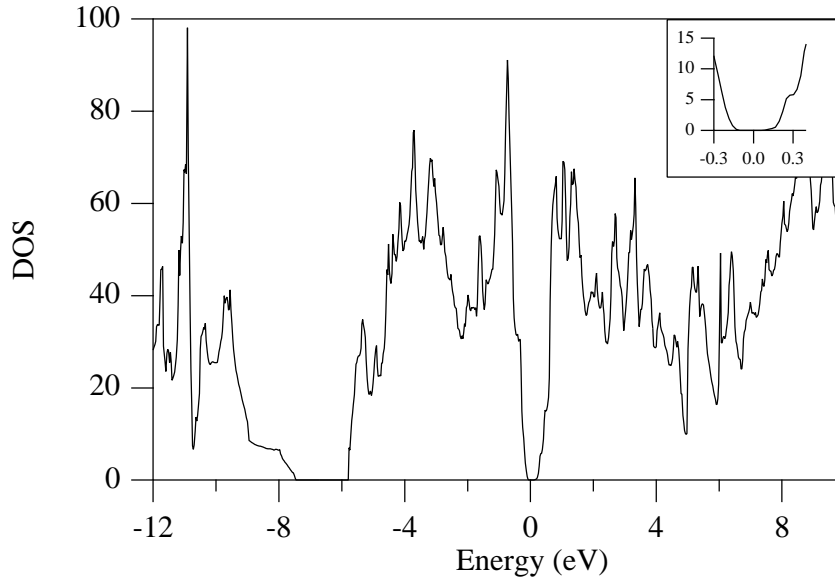
Fig. 4.7. The density of states of β-As$_2$Te$_3$. The inset shows a closer view near the Fermi energy.
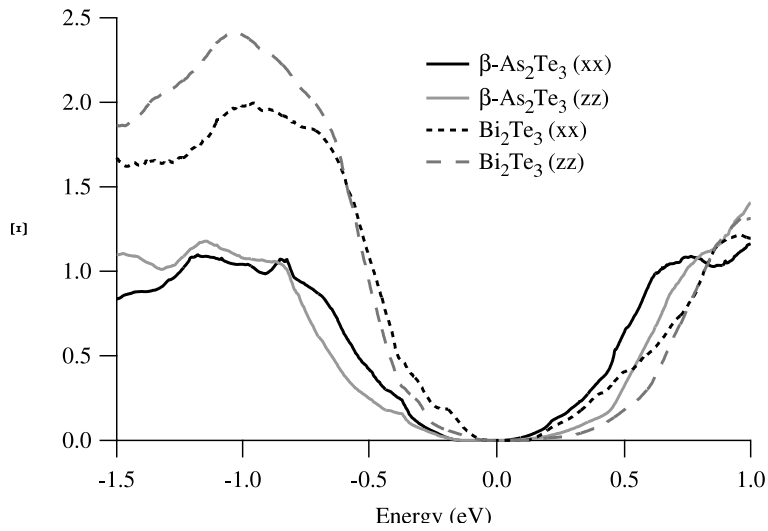
Fig. 4.8. The transport distribution of $\beta-$As$_2$Te$_3$ is shown along with that of Bi$_2$Te$_3$.

compete with Bi_2Te_3 or other present room temperature thermoelectric materials as a pure compound.

4.4 Conclusions

We have calculated the electronic structure of $\beta-As_2Te_3$ for comparison with that of Bi_2Te_3. Calculations reveal a band gap for $\beta-As_2Te_3$ which is slighly smaller than bismuth telluride's. The band structures are very similar with a small difference at Γ. Transport calculations also show qualitative similarities between the two compounds. Bi_2Te_2 shows a larger PF though, and with its low thermal conductivity would most likely have a larger figure of merit. Finally, we note that because of the similarities in the electronic structures, experimental studies are required to determine the amount of flexibility $\beta-As_2Te_3$ may provide for tuning the electronic structure of Bi_2Te_3.
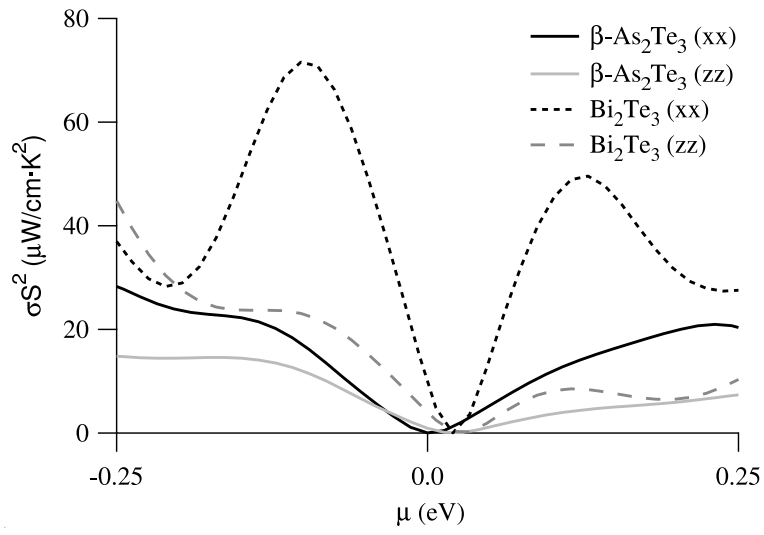
Fig. 4.9. The calculated power factors, using $\tau = 1.0 \times 10^{-14} s$, of $\beta-\mathrm{As_2Te_3}$ are shown along with those of $\mathrm{Bi_2Te_3}$.

Chapter 5

Thermoelectric Power of As_2Te_3
and Alloys Containing As_2Te_3 Under Pressure

5.1 Introduction

5.1.1 As_2Te_3

We pointed out in Chapter 1 that the trend of Group V and VI compounds used as room temperature thermoelectric materials seemed incomplete. Of all possible V-VI compounds, Bi_2Te_3 and Sb_2Te_3 seem to be the most thoroughly studied. Very little research, though, has been done on crystalline As_2Te_3. This is due, in part, to the fact that single crystals are nearly impossible to grow, and polycrystalline samples are difficult to grow. When they are grown, they are very weak [10, 36]. There are also handling difficulties because arsenic is very toxic.

Transport experiments on As_2Te_3 began 50 years ago when it was studied along with Bi_2Te_3 and Sb_2Te_3 [10, 36]. The electrical conductivity, thermal conductivity, and thermoelectric power of arsenic telluride were measured, but all proved to be unstable. Both p and $n-$type As_2Te_3 were found in the same ingot grown for the experiments. After these initial studies, crystalline arsenic telluride is found only scarcely in the literature.

Another reason As_2Te_3 may have received less attention is because its structure is different from the $R\bar{3}m$ space group of Bi_2Te_3 and Sb_2Te_3. At room temperature and

pressure, As_2Te_3 is monoclinic with spacegroup $C2/m$ ($\alpha-As_2Te_3$) [16, 46, 99]. Another phase of As_2Te_3, one that is isostructural with Bi_2Te_3, has been seen at high pressure and when $\alpha-As_2Te_3$ is quenched rapidly from high temperature. This phase is known as $\beta-As_2Te_3$. Here, starting with commercially available monoclinic arsenic telluride, we study its thermopower inside the DAC. No published experiments were found showing high pressure Seebeck coefficient measurements. Our ultimate goal of these experiments though, are to produce $\beta-As_2Te_3$.

A previously published phase diagram for As_2Te_3 is shown in figure 5.1 [49]. The authors only studied As_2Te_3 up to 1.7 GPA. At this pressure and room temperature, $\beta-As_2Te_3$ is not seen. In the P-T plane, the separation of the monoclinic and rhombohedral phases is linear in the ranges the authors studied. A rudimentary extrapolation would yield a room temperature phase transition near 7 GPa. Here, we attempt to see the β phase of arsenic telluride and measure its thermopower under pressure using a Mao-Bell DAC.

5.1.2 Alloys

The current market for thermoelectric devices is dominated by bulk alloys. Most room temperature applications use alloys containing bismuth, tellurium, antimony, and selenium. The best room temperature alloys have the composition $(Bi_2Te_3)_x$ $(Sb_2Te_3)_y$ $(Sb_2Se_3)_{100-(x+y)}$, where $x = 90$ and $y = 5$ for $n-$type material, and $x = 25$ and $y = 72$ for $p-$type material. Their figures of merit are near 1.0. Bi_2Te_3 and Sb_2Te_3 alone have figures of merit of 0.68 and 0.12 respectively. So, we see that alloying can have a large effect on transport properties.
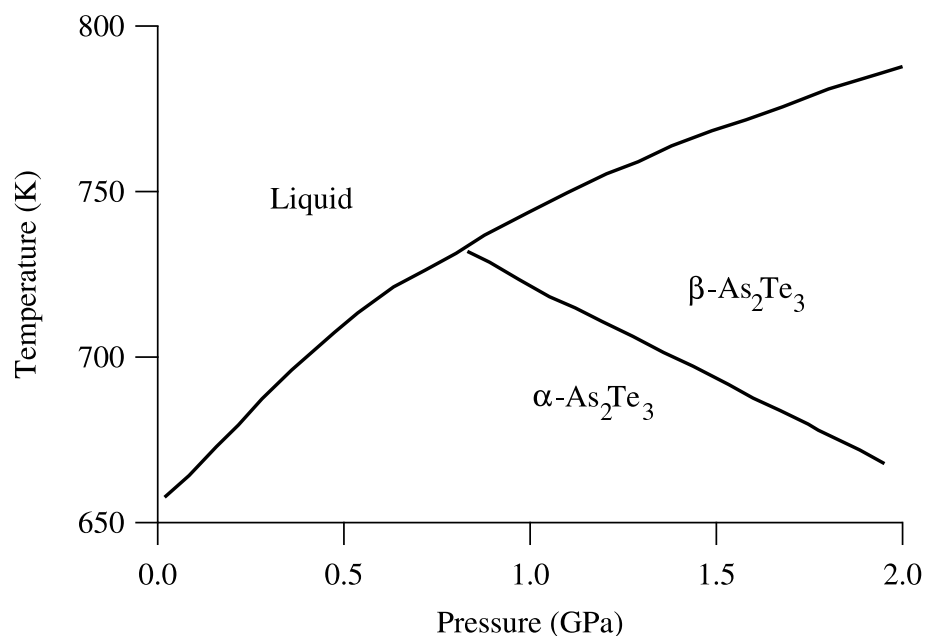
Fig. 5.1. High pressure and temperature phase diagram of As_2Te_3. The authors studied the structure up to only $1.7 GPa$.

There are two important effects of alloying on the structure, and hence electronic structure, of a compound [17]. First, the occupation of atomic sites by alloying atoms causes disorder in the normal periodicity of the structure. Second, shifting atoms away from their usual atomic sites causes positional disorder. Selenium is considerably smaller than the other constituents in the alloys mentioned above. Although it is difficult to predict the effects of alloying on a given material, this has a profound effect on the band structure, scattering of carriers, and hence the transport properties. Here we look at the effect of arsenic on known good room temperature thermoelectric material alloys.

Less than 1.0% As_2Te_3 is soluble in Bi_2Te_3 [108]. Since the best alloys contain antimony and selenium, both smaller than bismuth, it may be possible to form an alloy that contains a higher percentage of arsenic. Here we replaced some of the antimony and selenium in $(Sb_2Te_3)_{72}$ $(Bi_2Te_3)_{25}$ $(Sb_2Se_3)_3$ with arsenic and tellurium. We produced alloys of the form $(Sb_2Te_3)_{72}$ $(Bi_2Te_3)_{25}$ $(Sb_2Se_3)_x$ $(As_2Te_3)_{1-x}$ where $x = 0, 1, 2, 3$, and measured their thermoelectric powers under pressure. To observe the effect of As_2Te_3 versus Sb_2Se_3, alloys of the form $(Sb_2Te_3)_{75-x}$ $(Bi_2Te_3)_{25}$ $(As_2Te_3)_x$ $(x = 0, 1, 2, 3)$ were also synthesized.

5.2   Experimental Details

5.2.1 As_2Te_3

Pure As_2Te_3 was purchased from Alfa Aesar (99.999%) in pieces ranging from 1 to $15mm$ in any dimension. Samples were cut from larger pieces. The average sample

size for study in the DAC was $750\mu m$ L $\times$ $100\mu m$ W $\times$ $50\mu m$ D. Larger samples were studied outside of the DAC.

X-ray patterns were collected using a Rigaku RU-200 with a rotating molybdenum anode. The apparatus was modified to adapt to the DAC as discussed in chapter 2. The diffracted x-rays were exposed to Kodak DEF-182 direct exposure film held in a curved camera attached to the DAC. The exposed film was developed manually. The elliptical patterns were then collapsed using a scanner and software designed specifically for the DAC geometry [69].

Thermopower and resistance measurements in the DAC were performed using the methods shown in chapter 2. Measurements outside of the DAC were made by placing the thermocouples between two samples of the same size. The sample was then laser-heated with IR radiation on its end to eliminate instability due to radial temperature gradients. This set-up proved extremely reliable for measurements outside of the DAC. In the DAC, IR radiation was focused as a line to heat the sample. The heating of all samples was visualized using a CCD camera sensitive to IR radiation. The voltages across the thermocouple legs were measured simultaneously using two digital nanovolt meters and LabView. Resistance measurements inside the DAC were made using the thermocouples from the thermopower measurements in a pseudo-four configuration.

Pressure measurements were made using the ruby florescence method (chapter 2) with a He-Ne laser of wavelength $\lambda = 543.5nm$. Optics were configured to allow visualization, heating, and pressure measurements to be collected concurrently.

5.2.2 Alloys

The alloys studied were obtained from the chemistry department at Cornell University [64]. The binary constituents were crushed and weighed to give the proper stoichiometric proportion. The powder was pressed into small cylindrical pellets which were then annealed at $250^{\circ}C$ for three weeks.

Ambient pressure thermopower measurements were made by pressing the chromel-alumel thermocouples between two samples of the same size ($4mm$L $\times$ $0.5mm$W $\times$ $0.25mm$T). This ensured good thermal contact and minimized the effect of non-uniform transverse temperature gradients. Heating the sample from the side (along the sample axis) also helped to create a purely axial thermal gradient. The sample was laser-heated and the thermopower was measured using the same equipment and arrangement described in chapter 2. The resistance of the samples in the DAC was measured using the thermocouples in a pseudo-four probe configuration. The crystal structures were determined from x-ray diffraction patterns using Le Bail refinement [77].

5.3 Results and Discussion

5.3.1 As_2Te_3

Just as reported by J. Black, et al., we found n and $p-$type As_2Te_3 within the same sample ingot [10]. For consistency, we selected samples with similar ambient pressure thermopowers for all experiments. All samples placed under pressure in the DAC had thermopowers between $-240\mu V/K$ and $-255\mu V/K$ at ambient pressure.

Under pressure, one trend in the measured Seebeck coefficient and resistance was consistently reproducible. The thermopower results are shown in figure 5.2 (Sample 1). The absolute value of the thermopower was found to decrease quickly to $S \approx 60\mu V/K$ near 4 GPa. It then dips back down and tends steadily toward $S \approx 25\mu V/K$. Looking more closely near 6 GPa though, a slight kink can be seen. Though this is not obvious evidence of some type of transition, the structure of the data from a another sample near the same pressure is more revealing (Sample 2 in figure 5.2).

The resistance data for the sample 2 is shown in figure 5.3. The behavior shown is typical of semiconductors under pressure in the DAC. The resistance drops quickly as the gap, most likely, begins to close. Again, near 6 GPa, a kink in the trend, more obvious than in the thermopower data, is visible. This could be evidence of a structural or electronic topological transition. Assuming that size effects are minimal as the pressure is increased, this decrease in resistance is consistent with a transition from a monoclinic semiconductor to a semiconductor with a more ordered structure. X-ray diffraction was used to investigate the possibility of a phase transition.

X-ray diffraction patterns of As_2Te_3 at 4 and 8 GPa are shown in figure 5.4. A phase transition has occurred between the two pressures. Using the 8 GPa pattern, we calculated hexagonal unit cell parameters of $a = 3.83\mathring{A}$ and $c = 30.10\mathring{A}$ [81]. This corresponds to a unit cell with volume $V = 382.9\mathring{A}^3$. This calculated volume is 9.2% smaller than that found experimentally in reference by Toscani, et al. [99]. The results are consistent since the authors used data obtained at ambient pressure to refine the structure of $\beta-As_2Te_3$.
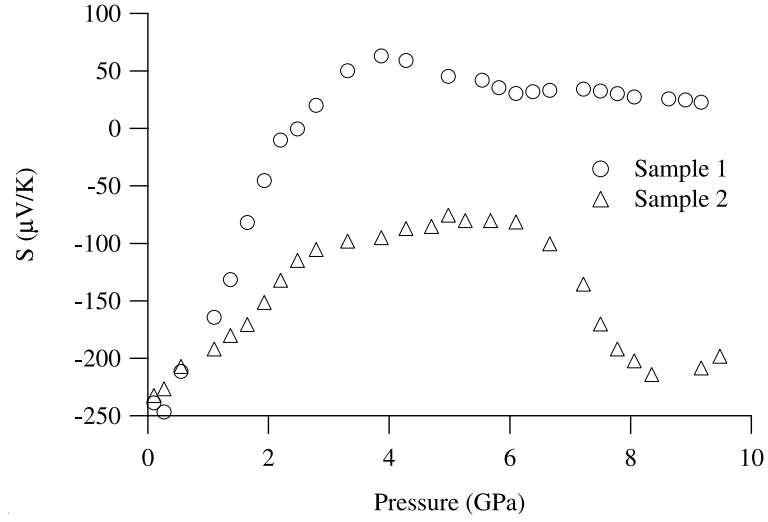
Fig. 5.2. The thermoelectric power of pure As_2Te_3 is plotted versus pressure.
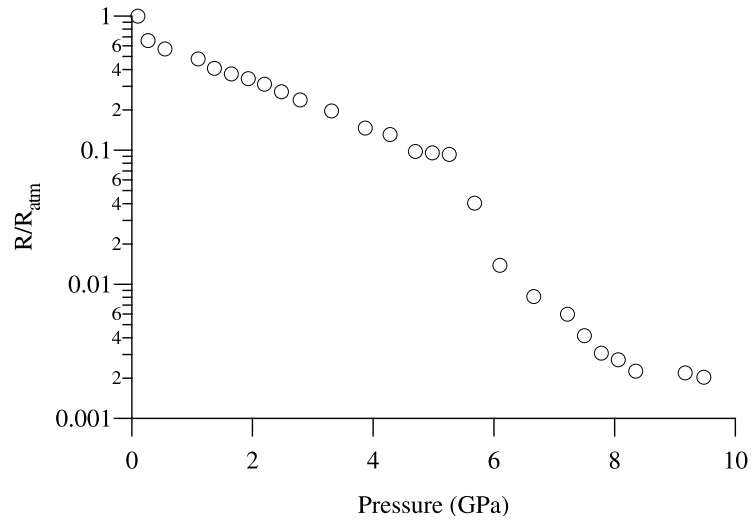
Fig. 5.3. The logarithm of the resistance with respect to atmospheric pressure resistance of As_2Te_3 is plotted against pressure.
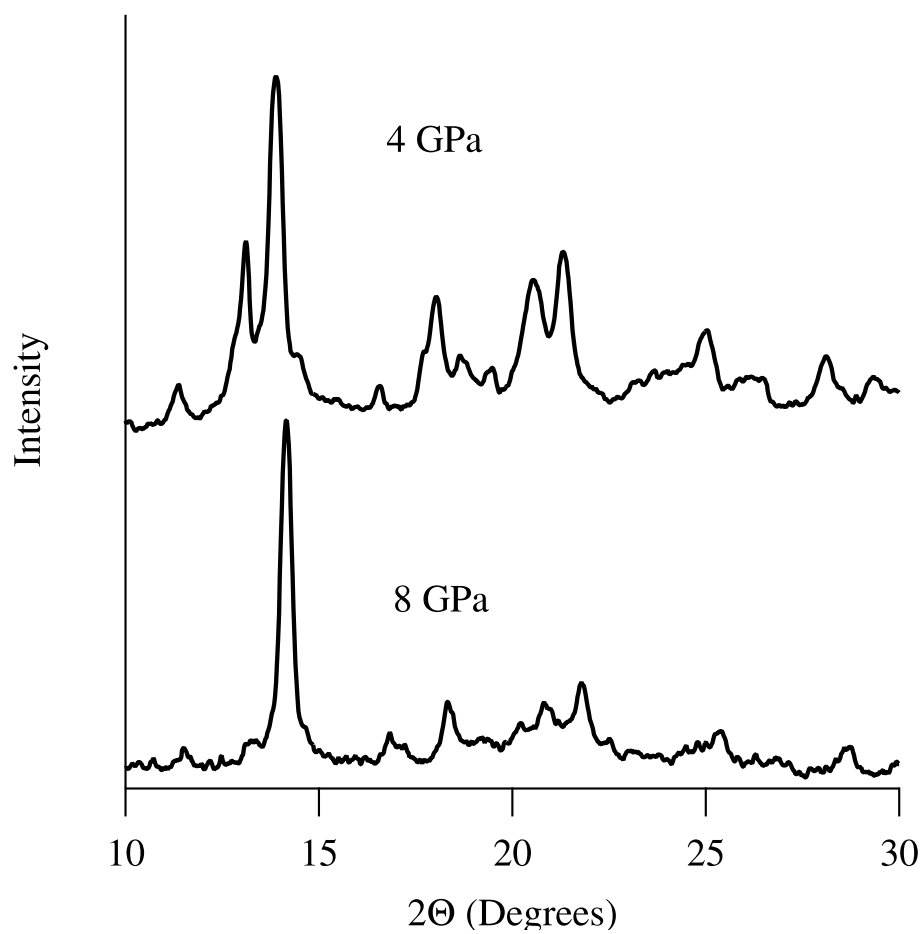
Fig. 5.4. X-ray diffraction patterns at 4 GPa and 8 GPa.

5.3.2 Alloys

The only alloys that sintered well enough to withstand pressure tuning, were containing those containing 0% and 1% As_2Te_3. The powder diffraction pattern for $(Sb_2Te_3)_{72}$ $(Bi_2Te_3)_{25}$ $(Sb_2Se_3)_2$ $(As_2Te_3)_1$ (alloy c) is shown in figure 5.5. Le Bail refinement gave cell parameters of $a = 4.2907\mathring{A}$ and $c = 30.4624\mathring{A}$. This has a larger unit cell than the pseudo ternary alloy $(Sb_2Te_3)_{72}$ $(Bi_2Te_3)_{25}$ $(Sb_2Se_3)_3$. This was expected, comparing the constituents in table 1.2. The alloys we produced were not optimally doped, but our room pressure result, $S = 225\mu V/K$, agrees with the published thermopowers [29, 109].

$(Sb_2Te_3)_{72}$ $(Bi_2Te_3)_{25}$ $(Sb_2Se_3)_3$ (alloy D), the best known $p-$type alloy in this family, was pressure tuned up to 12 GPa (figure 5.6). The thermoelectric power decreases rapidly to a local minimum of $S = 14\mu V/K$ at 5.25 GPa. It then increases slightly before a kink appears between 6 and 8 GPa. This is due to a phase transition in Sb_2Te_3 that is known to occur at 7.3 GPa [48, 80]. Having good agreement between our ambient pressure thermopower and other published values, and having reproduced a known first order phase transition, we then pressure tuned our alloy containing 1% As_2Te_3.

Alloy C was also pressure tuned up to 12 GPa (Figures 5.7 and 5.8). The two most reproducible experiments are shown as sample 1 and 2. Both samples show slightly different trends as their thermopowers decrease nearing the phase transition point at 7.3 GPa. After the transition both samples are in nearly exact agreement. Other than the phase transition being more obvious in alloy d above (figure 5.6), the thermopower
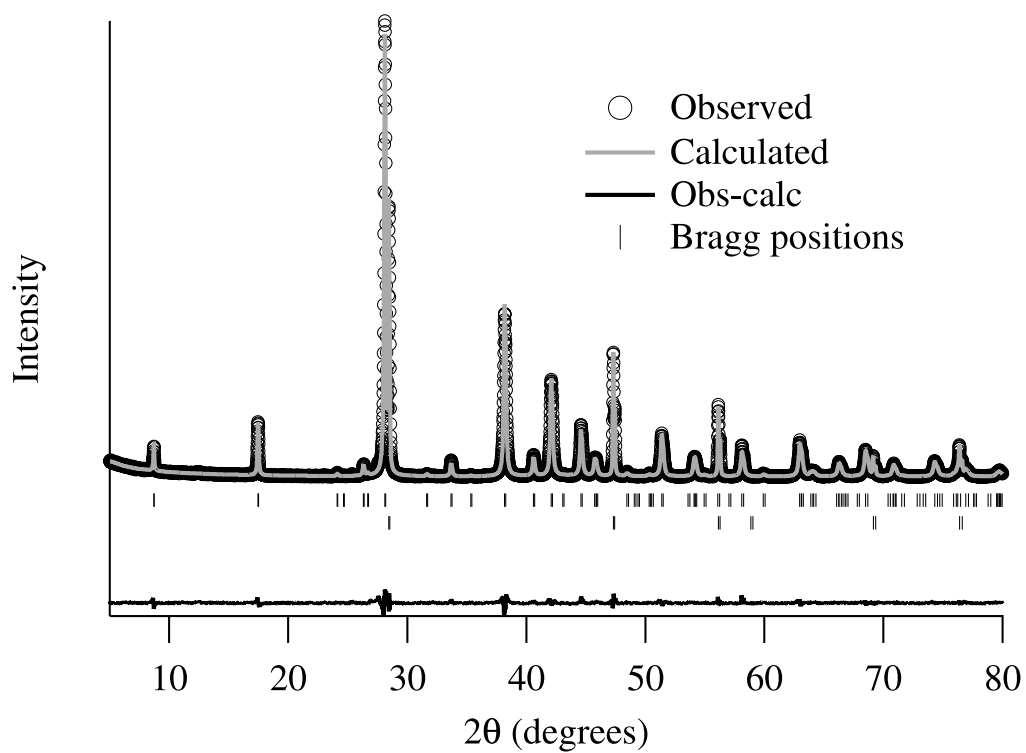
Fig. 5.5. Diffraction pattern of $(Sb_2Te_3)_{72}$ $(Bi_2Te_3)_{25}$ $(Sb_2Se_3)_2$ $(As_2Te_3)_1$. Refinement yielded cell parameters of $a = 4.2907\text{Å}$ and $c = 30.4624\text{Å}$.

results for alloy c and alloy d are very similar. The resistance data show typical behavior for these experiments.

From alloy C and D data, it is apparent that there is no enhancement of their thermoelectric properties due to pressure. At ambient pressure, the thermopower of alloy D is greater than the thermopower of alloy c. Alloy C has the larger cell volume of the two. To see how much structural freedom the addition of arsenic telluride does actually offer, we synthesized four other alloys. These new alloys contained no Sb_2Se_3, only Sb_2Te_3 Bi_2Te_3 and As_2Te_3. The alloys were of the form $(Sb_2Te_3)_{72}$ $(Bi_2Te_3)_{25}$ $(As_2Te_3)_x$, where $x = 0, 1, 2, 3$. The volumes of the different alloy unit cells, with and without Sb_2Se_3, are shown in figure 5.9. We can see that As_2Te_3 does not lower the cell volume as much as Sb_2Se_3 alone.

5.4 Conclusions

The thermopower of As_2Te_3 has been measured up to 10 GPa in a Mao-Bell DAC. The transport and x-ray diffraction data show that a phase transition occurs near 8 GPa. The data presented shows a thermopower indicative of a rhombohedral (Group V-VI) semiconductor, similar to Sb_2Te_3 and Bi_2Te_3, at high pressure. Since arsenic is much smaller than bismuth and antimony, we expect the lattice thermal conductivity in As_2Te_3 to be much higher than in Sb_2Te_3 and Bi_2Te_3 [73]. Though not evident in this work, high pressure may still provide a route to alloys that could reproduce the behavior of $Sb_{1.5}Bi_{0.5}Te_3$ reported by Badding, et al. with further tuning [73].

It is difficult to say whether the Sb_2Se_3 in presently used alloys has the same structural effect as that which produced an increase in thermopower found by Badding,
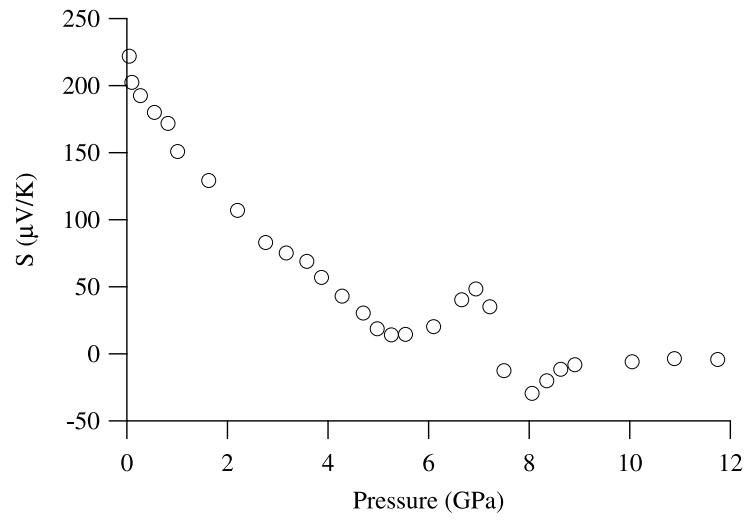
Fig. 5.6. Thermoelectric power of Alloy D under pressure.
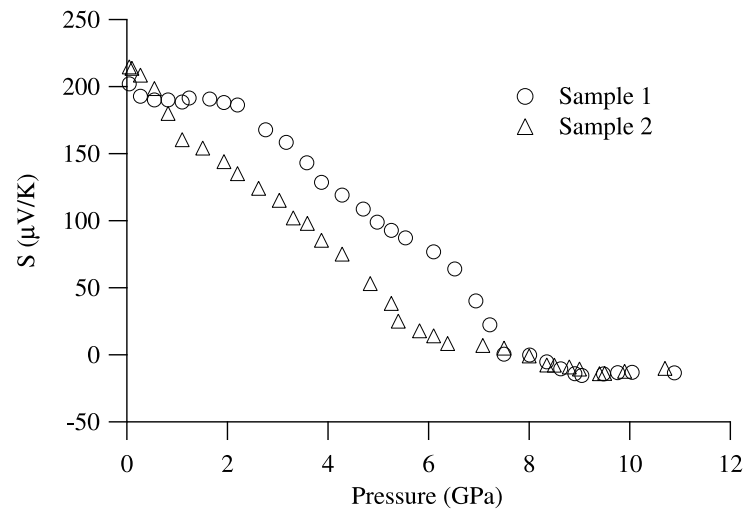
Fig. 5.7. Thermoelectric power of Alloy C under pressure.
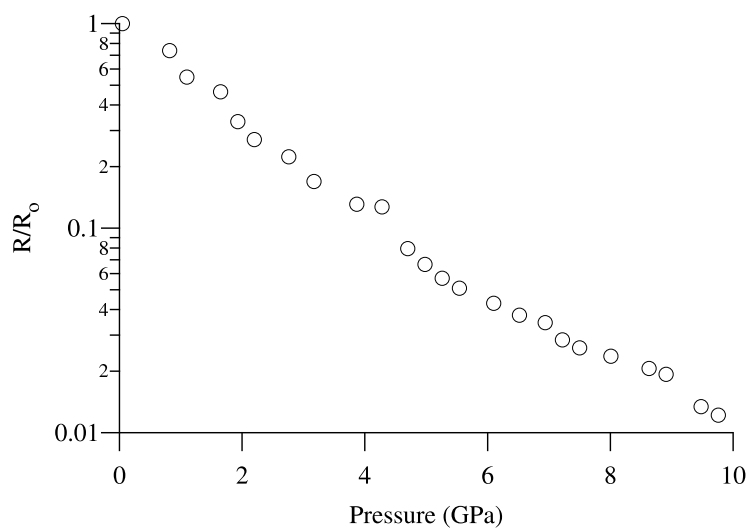
Fig. 5.8.   The logarithm of the relative resistance of Alloy C under pressure.
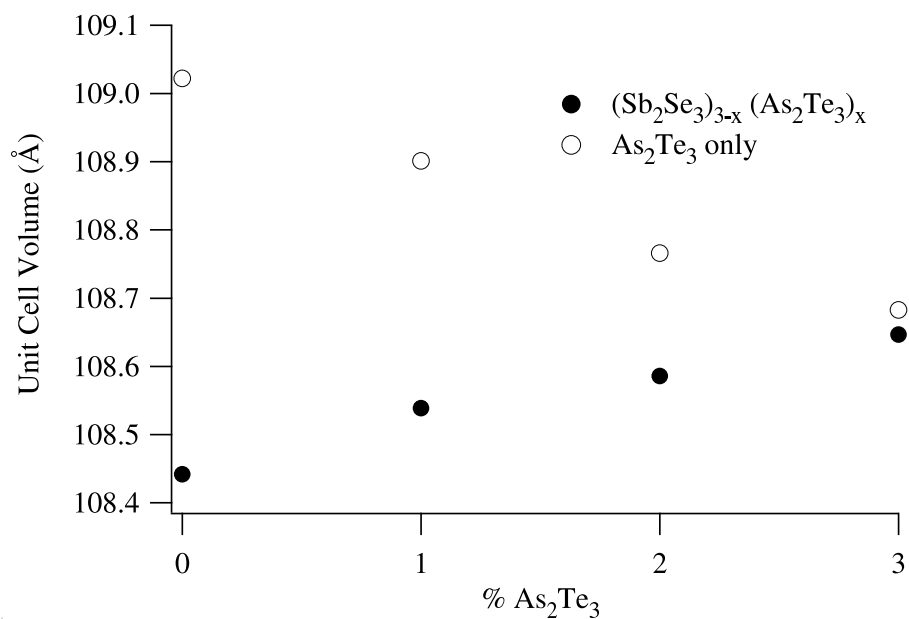
Fig. 5.9.   Unit cell volumes for alloys containing both As_2Te_3 and Sb_2Se_3, and those containing As_2Te_3 only.

et al. [73]. We saw that from a structural standpoint, arsenic telluride could provide only little extra freedom in presently used alloys. The high solubility of Sb_2Se_3 in Sb_2Te_3 and Bi_2Te_3, and the high toxicity of arsenic though, will likely keep alloys of bismuth, antimony, tellurium, and selenium the predominant room temperature thermoelectric materials.

Chapter 6

Low-Dimensional Structures
in Silica Hosts

6.1 Introduction

Previously we have focused on bulk alloys that are used in room temperature thermoelectric devices. Bulk materials are preferred for large scale cooling because their production is relatively easy. Now we turn to low-dimensional thermoelectric structures. They are more difficult to produce for large scale cooling, but there are three advantages in their use over current commercially produced bulk materials. Lowering the dimensionality enhances the density of states near the Fermi energy, creates phonon scattering at the interfaces (leaving the carriers less affected), and some semimetals undergo a transition in which a band gap opens and the compound becomes semiconducting.

The figure of merit of a compound depends on its band structure near the Fermi energy. We saw this manifested by way of the transport distribution (TD) introduced in chapter 3. The best TD for thermoelectric performance is a delta function or a step function [62, 96]. The density of states, on which the TD depends, of a two-dimensional material, or thin film, has very different behavior than a bulk material. For example, in the case of parabolic bands, a two-dimensional structure would have a DOS with the form of a step function (Figure 6.1). This can greatly increase the figure of merit compared to the same material in bulk form.
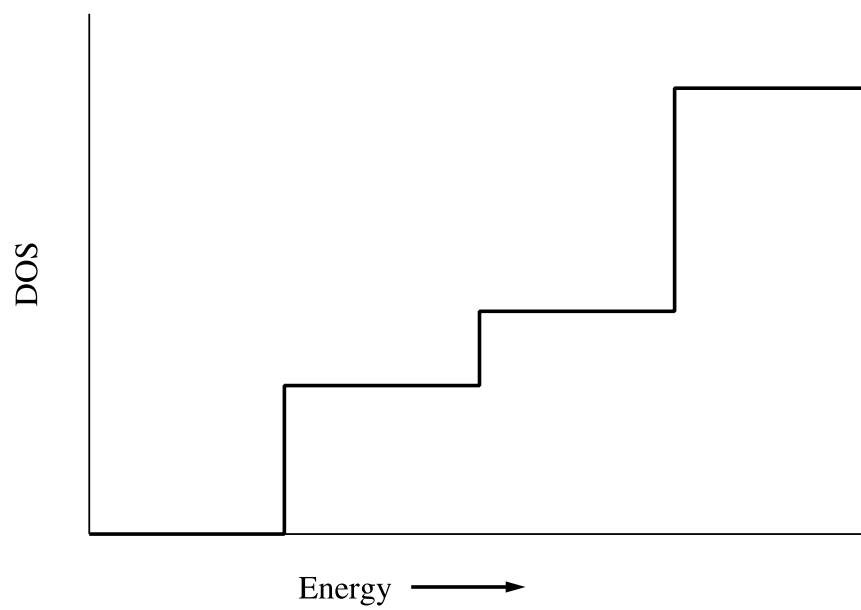
Fig. 6.1. A general density of states for a two dimensional quantum well. Each step is due to the next sub-band (which overlaps the previous bands) with increasing energy.

The figure of merit also depends on the thermal conductivity of the lattice. This is a major contributing factor to the success of Bi_2Te_3 alloys as thermoelectric materials. They have very low thermal conductivities. Considerable lowering of the thermal conductivity, due to phonon scattering at interfaces is apparent in superlattices [102]. The low thermal conductivity due to "phonon-blocking/electron-transmitting" structures, combined with the enhanced DOS can significantly improve ZT beyond that obtained in bulk materials.

Semiconductors are the best thermoelectric materials [62, 89]. It has been predicted that nanowires of bismuth, which is a semimetal in bulk form, becomes semiconducting when the diameter of the wires are 50 nm or less [23]. Alloying with antimony may cause this transition at a larger diameter [57]. In either case, this would greatly enhance the thermoelectric figure of merit of the nanowires.

Several theoretical and experimental examples of such low dimensional thermoelectric structures have already been published [13, 24, 26, 31, 41, 42, 94, 102]. Most of the nanowires used in these experiments are embedded in a host material, usually porous alumina. The material is deposited inside channels in the hosts by either electrochemical deposition, pressure injection or the vapor phase method. Within the last two years superlattice nanowires have also been fabricated using the vapor-liquid-solid (VLS) growth mechanism [9, 35, 105]. These experiments have shown figures of merit greater than $ZT = 2$ [37, 102].

The systems that have shown such high figures of merit though, are not practical commercially [24]. They are too expensive and too complex for mass production and for large scale cooling. Some advances have been made toward a more feasible solution, but

filling factors of the hosts are still not high enough and the thermal conductivity of the hosts are still not low enough [74]. In this chapter we set forth a possible solution.

Our materials were deposited in silica (SiO_2) hosts. At room temperature, silica has a thermal conductivity of $\kappa = 0.033 \frac{W}{m \cdot K}$. This is twenty-one times lower than the lattice thermal conductivity of Bi_2Te_3. This is definitely low enough so as not to inhibit the thermoelectric cooling or power generation of a material embedded in the silica. It remains to demonstrate the flexibility of such silica hosts. That is the goal of this chapter.

These porous silica hosts can also be used as an experimental tool. Silica fiber have very high tensile strengths. In previous chapters we discussed pressure tuning in which samples are compressed. The fiber hosts also provide a means to place thermoelectric materials under tension. After a material has been deposited in the hosts, the fiber can then be stretched, in turn stretching the resident material.

First we will summarize the methods by which we deposit different semiconductors into the silica hosts. Silicon, germanium, and arsenic were deposited in several types of holey silica fibers. The interest in silicon and germanium is due to their potential as a high temperature power generator [25, 52]. Our interest in arsenic is two-fold. First, there are trends in group V elements which extend from bismuth to antimony to arsenic [45]. Currently there is much interest in bismuth and antimony nanowires and thin films [24, 40, 74]. Even though we have not yet deposited bismuth into these silica hosts, arsenic could provide some insight into the potential of thin films of antimony and bismuth in such hosts. Arsenic may also be beneficial thermoelectrically in itself. For thin films of bismuth, as the quantum well width decreases, a semi-metal to semiconductor

transition occurs [23, 57]. The same may also hold true for antimony, arsenic, or alloys of the two elements.

Although several different sizes of capillaries have been fabricated and "filled", we use fibers with an average capillary diameter of $2\mu m$ for measurements. This is obviously not on the nano-scale, but we deposit the semiconductors in the form of thin films. These thin films are deposited annularly inside the silica capillaries. We then present results of thermopower measurements of silicon deposited in the large air fraction fibers. Measurements were made on arrays of 400 to 500 annularly filled "tubes".

6.2 Experimental Methods

6.2.1 Deposition

The porous fibers were obtained from the Optoelectronic Research Centre (ORC) at The University of Southampton [82]. The fibers were fabricated in a manner similar to that described in the literature [44, 50, 51, 79, 98]. In the process of being drawn, the fibers are coated with a protective acrylic coating. This protects the fibers from scratching and moisture during handling while being prepared for filling.

For deposition in the porous fibers, a pressure injection method was used [83]. Semiconductor grade gases - silane (SiH_4), germane (GeH_4), and arsine (AsH_3) - were used as precursors. Argon and helium were used as carrier gases. The precursor-carrier gas mixture was loaded into a stainless steel reservoir. The porous silica fibers were then secured, using a high pressure connection, to the precursor-carrier gas reservoir. The

fiber was placed in a 3600 W resistive tube furnace to attain the required temperatures for the decomposition reactions.

6.2.1.1 Germanium

A mixture of 5% germane and 95% argon was injected into the silica host, which had a 2 μm inner diameter, at a pressure of 3150 pounds per square inch ($p.s.i.$). The temperature of the host and precursor was ramped to $425^{\circ}C$, in a 75 cm tube furnace, from room temperature, over three hours. The host was kept at $425^{\circ}C$ for 21 hours. At this time, flow of the gas mixture had ceased.

6.2.1.2 Silicon

5% silane with 95% helium was injected into a 2 μm capillary, and a large air fraction fiber with 2 μm channels at a pressure of 3500 $p.s.i.$ In the case of the capillary, the precursor/carrier mixture was allowed to flow while the temperature of the host was ramped to $700^{\circ}C$ from $300^{\circ}C$ over 220 min. After reaching $700^{\circ}C$, deposition was allowed to proceed for 90 min. In the case of the large air fraction host, helium was flowed while the temperature was brought to $700^{\circ}C$. A 75 cm tube furnace was used here as well. Flow was then switched to the gas mixture. The reaction was allowed to proceed until gas flow had stopped as indicated by visually observing flow from the host.

6.2.1.3 Arsenic

For deposition of arsenic, 3.3% arsine mixed with 96.7% helium was injected into a 2 μm capillary host at a pressure of 2900 $p.s.i.$. In order to concentrate the deposition

over a shorter range in the capillary, a 2 cm resistive tube furnace was fabricated. The precursor-carrier gas mixture was allowed to flow while the temperature of the host was ramped to $350^{\circ}C$ from room temperature over 90 min. After reaching $350^{\circ}C$, deposition was allowed to proceed for 10 min.

6.2.2 Analysis

Deposition was confirmed using visible Raman spectroscopy to determine crystallinity and scanning electron microscopy to determine the film thickness. Raman scattering was performed with an argon-ion laser of excitation wavelength $\lambda = 514.5\ nm$. This wavelength was suitable for all samples, as none of them fluoresce near it. SEM images were taken using an FEI-Philips XL-20 microscope with energy dispersive x-ray analysis to verify the sample constituents.

6.3 Results and Discussion

6.3.1 Hosts

Several types of porous and capillary fibers were received from the ORC. The single capillaries ranged from $200nm$ to $5\mu m$ in inner diameter (Figure 6.2 shows a 2 μm inner diameter capillary). Other silica fibers were formed containing arrays of pores in different configurations. The holey fibers contain randomly oriented pores of various sizes ranging from $100nm$ to $8\mu m$ (Figure 6.3). Honeycomb or "large air fraction" fibers contain a more uniform array of pores of more consistent sizes. The pores in these fibers are closely packed hexagons, with diagonals of $2\mu m$ (Figure 6.4).
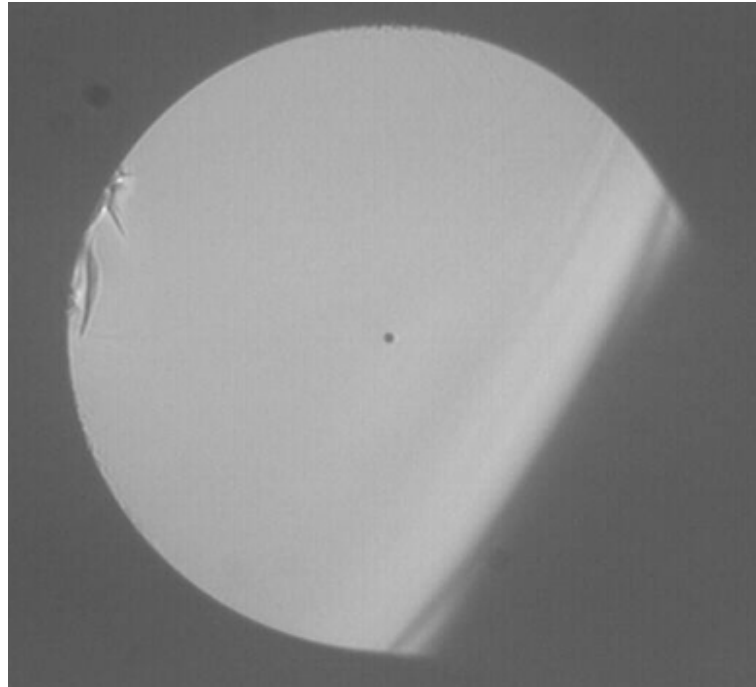
Fig. 6.2.   The capillary fiber has one hole through the center of the fiber. The outer diameter of the fiber is $150\mu m$ and the inner diameter is $2\mu m$.
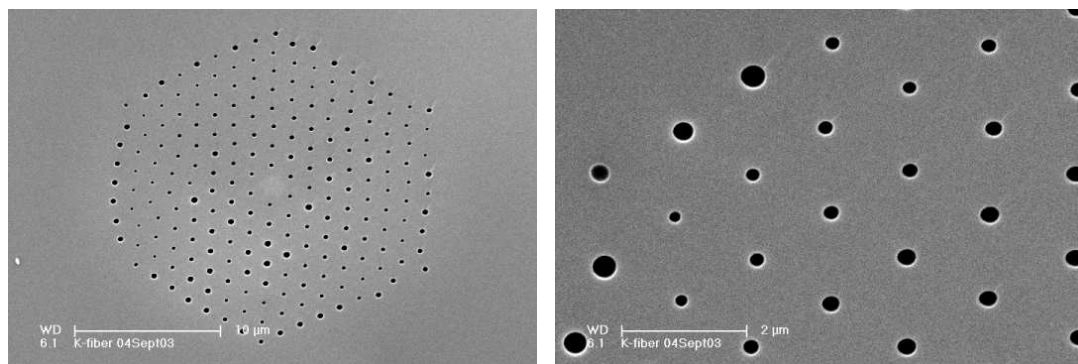
Fig. 6.3.   The holey fiber has an array of many pores ranging from 150 to $500nm$. The right photo is a close-up of the left photo. These pores are not packed as closely as the honeycomb fiber (Figure 6.2).

6.3.2   Deposition

6.3.2.1   Germanium

Thin film deposition over 20 cm or more is possible while keeping the film thickness uniform within 20%. Figure 6.5 is a scanning electron microscope image showing the cross section of a capillary coated with a 100 nm film of germanium. The germanium thickness in the fiber shown was within 10% of 150 nm over a length of 17 cm of fiber and stayed within 20% over a length of 25 cm. A typical deposition profile of a capillary that was filled with germanium until gas flow ceased is shown in figure 6.6. Conditions were the same as above except that deposition was allowed to proceed for two days. The results are quite different if deposition is allowed to continue unchecked.

6.3.2.2   Silicon

SEM images of a silicon filled capillary, in which deposition was allowed to proceed until flow stopped, revealed that 75% filling of the capillary had occurred over a length of more than 21 cm. Figure 6.9 shows a cross section of the capillary where it is more than 85% filled. Using helium as the carrier gas, the deposition profiles are much smoother (Figure 6.7) than the profiles of experiments using argon as the carrier gas (Figure 6.8).

Silicon was also deposited in silica hosts with the pores arranged in a hexagonal packing configuration (Figure 6.4) as shown in figure 6.10. The thermoelectric power was measured for some of these samples. A thermopower of $S \sim -550 \ \mu V/K$ was measured for two samples which agrees with bulk silicon measurements. This was expected since the structures were on the order of or greater than 600 nm thick.
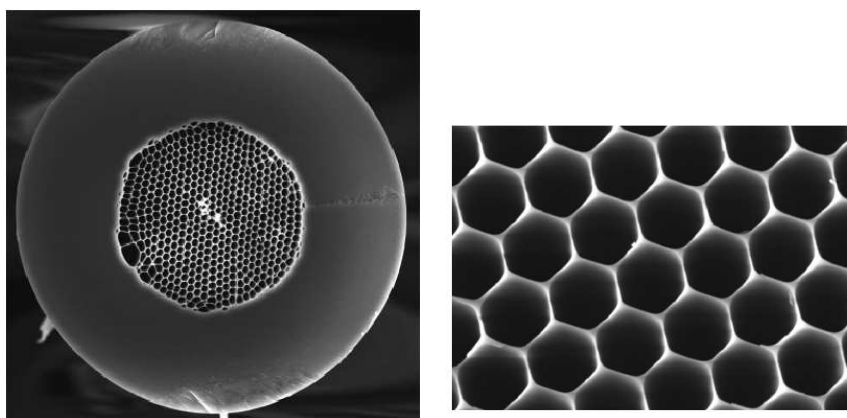
Fig. 6.4.   A view down the axis of a honeycomb-porous fiber is shown on the left with a close-up of the pores on the right.   Each pore is $2\mu m$ across the short axis of the hexagons.
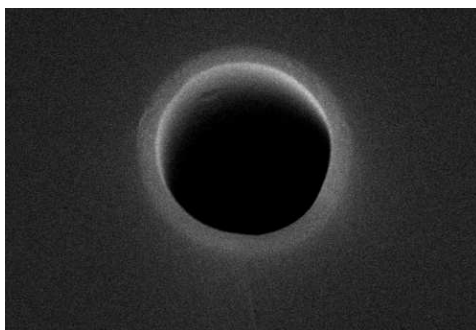
Fig. 6.5.   A 150 nm film coats the inner wall of a silica capillary with a 1.6 μm inner diameter. The silica cladding is darker surrounding the lighter inner germanium ring.
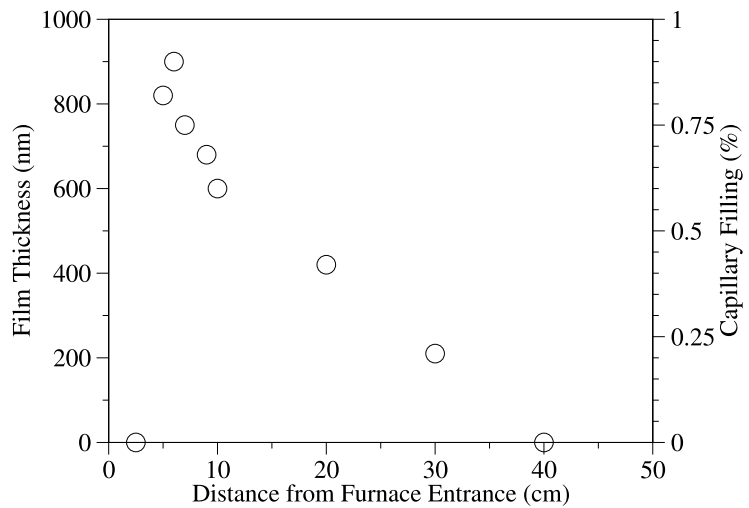
Fig. 6.6. The deposition profile for a germanium filled fiber using a GeH_4/Ar mixture is shown. The distances are from the furnace entrance. The tube furnaced used is 70 *cm* long.
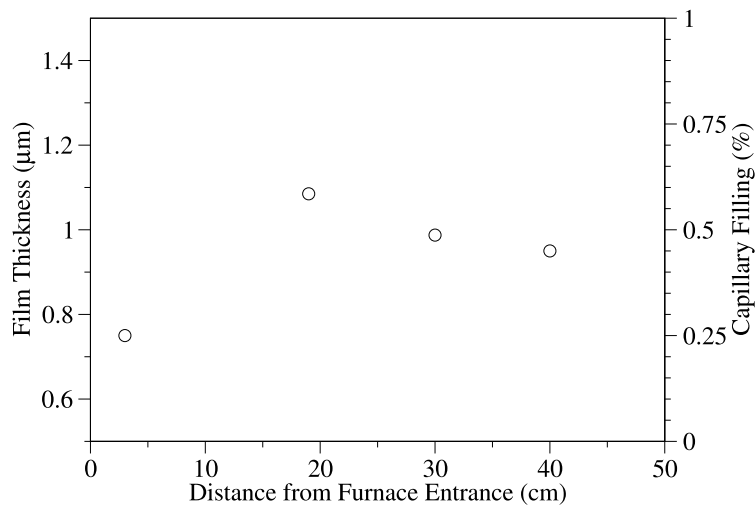
Fig. 6.7. The profile of a silicon "filled" fiber in which helium was used as the carrier gas is much smoother than profiles in which argon was used.
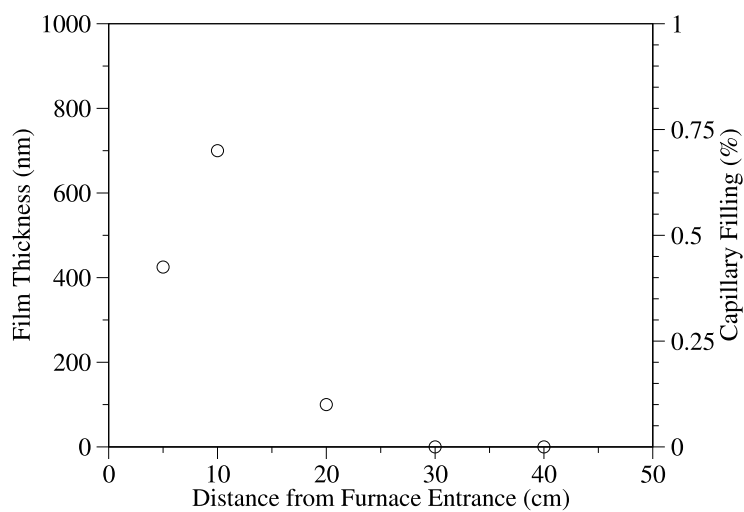
Fig. 6.8. The profile of a silicon "filled" fiber where argon was used as the carrier gas.
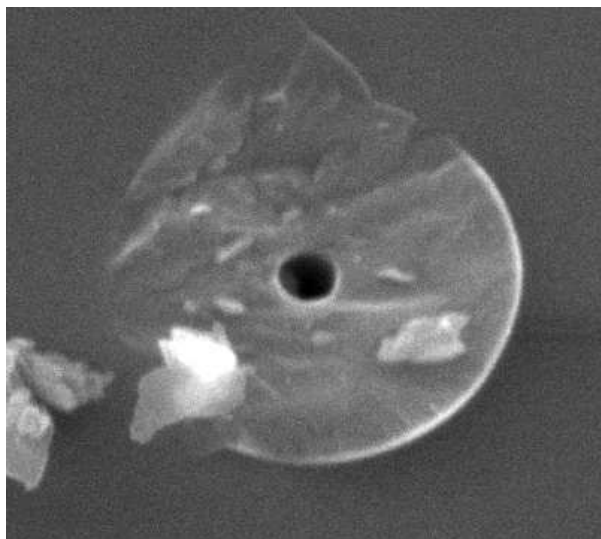
Fig. 6.9.   Here, a silica capillary that is more than 85% filled with silicon is shown. The lighter contaminants on the wire and silica cladding are remnants of the protective coating that are left behind after cleaving the fiber.
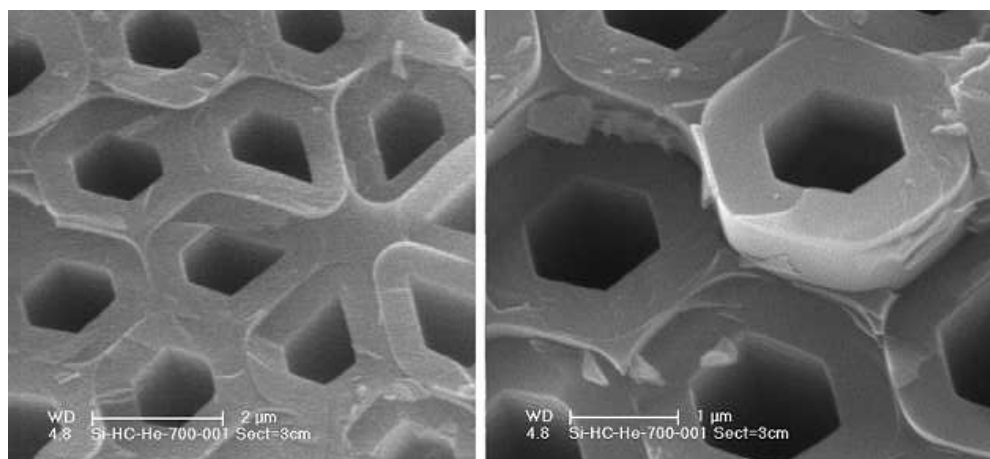
Fig. 6.10.   Slightly distorted hexagonal tubes of silicon are at the core of the silica fiber (left). A closer view reveals shards of the silica ribs between the tubes (right).

6.3.2.3 Arsenic

The most recent successful experiment was the deposition of arsenic in a 2 μm capillary. Inspection of the filled host with an optical microscope revealed that deposition had occurred over a length of less than 1 mm. This was expected since the experiment was conducted in a 2 cm tube furnace. Raman spectroscopy confirmed the presence of crystalline arsenic in the silica fiber host (Figure 6.11). The peak positions are in exact accordance with other published results on pure arsenic (Table 6.1) [55]. The intensities of the peaks are reversed though. This could be due to stresses in the arsenic crystals or heating as a result of the incident laser light.

6.4 Conclusions

We have presented results that show the feasibility of depositing low-dimensional semiconductors and a semimetal in microscale porous silica hosts. Films in the range of 50 nm to 1 μm were regualrly attainable. Silicon, germanium, and arsenic have all been successfully deposited. The silica hosts are already produced on a large scale. We have shown that deposition in these hosts using hydride precursors is a simple process. New deposition techniques for other materials are already being developed for these silica structures. The methods and hosts used are new to the field of thermoelectrics, and experiments with these hosts are continuing.
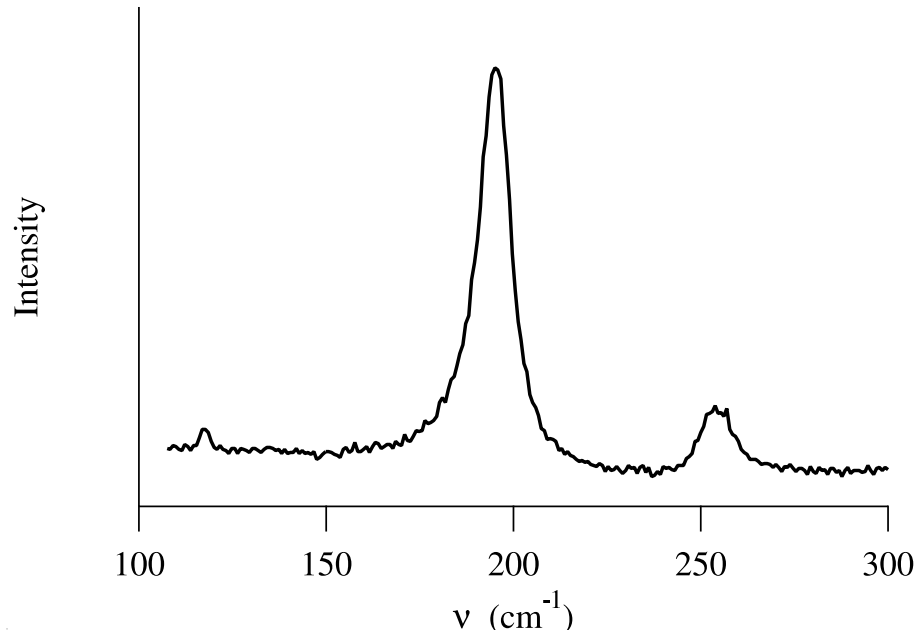
Fig. 6.11.   The Raman spectrum of arsenic showing the As-As stretch (253.8 cm^{-1}) and anti-stretch (195.0 cm^{-1}) modes [75].

Table 6.1.
First-order Raman peaks of arsenic [55].

Peak	ω (cm^{-1})	Intensity
Stretch	254.3	1.00
Anti-Stretch	193.5	0.33

Chapter 7

Conclusions

There are three goals of the research described in this manuscript. First and most general, we wanted to study the impact of arsenic on group V-VI thermoelectric materials. Second and more specifically, we wanted to determine whether its impact could improve the efficiency of those materials. Several techniques were used in the investigation and several beneficial results were obtained. Finally, we investigated a new host for low-dimensional thermoelectric structures.

In chapters 2 and 3 we described two methods used to tune thermoelectric materials or find new ones. Pressure tuning provides a way to scan phase space rapidly and determine if any thermoelectric improvements can be found in a given compound. Measuring transport properties, laser heating, x-ray diffraction, and Raman spectroscopy all contribute to the value of the DAC.

Using first-principles calculations to estimate transport coefficients provides a different angle to improve thermoelectric materials. With only very little information (the crystal structure of the compound in which one is interested), we can gain insight into the materials' worth as a thermoelectric. Whereas modeling provides invaluable tuning capabilities of well known compounds, first-principle calculations can provide assistance in the search for new thermoelectric materials.

Though arsenic telluride is not a new compound, the rhombohedral phase $\beta-As_2Te_3$, has not been studied from a transport point of view. Using the FP-LAPW method, in chapter 4, we calculated the band structure and ultimately some transport properties of $\beta-As_2Te_3$. From the calculated band structure, it seemed apparent that $\beta-As_2Te_3$ would have properties similar to Bi_2Te_3 and Sb_2Te_3. Though the trends in the transport distribution were similar near the band gaps of Bi_2Te_3 and $\beta-As_2Te_3$, Bi_2Te_3 has a power factor larger by a factor of four. Since $\beta-As_2Te_3$ likely has a higher thermal conductivity than Bi_2Te_3 because arsenic is much smaller than bismuth, it would probably not be able to compete with currently used room temperature thermoelectric materials.

In chapter 5 we used the diamond anvil cell to produce $\beta-As_2Te_3$ from monoclinic $\alpha-As_2Te_3$. Thermoelectric power and resistance measurements showed either a phase transition or electronic topological transition near $7\ GPa$. X-ray diffraction experiments confirmed a phase transition between $4\ GPa$ and $8\ GPa$. Here we proved that high pressure alone provides a route to $\beta-As_2Te_3$, whereas previously published reports used high temperature.

Since the binary compound alone could not compete as a thermoelectric material, we also synthesized alloys of group V-VI compounds containing As_2Te_3. In chapter 5, we showed that As_2Te_3 is more soluble in alloys of bismuth, antimony, tellurium, and selenium, than in Bi_2Te_3 or Sb_2Te_3 alone. Although pressure tuning did not show any substantial benefits of alloys containing As_2Te_3, analysis showed that As_2Te_3 provides extra structural freedom. As_2Te_3 and Sb_2Se_3 combined may provide a route to a structure recently reported that showed an increase in thermopower of antimony-bismuth-tellurium alloys under pressure [73].

Finally in chapter 6 we explored a new host for low-dimensional thermoelectric materials. Recently research in this area has been stalled due to a lack of feasibility of currently used hosts in low-dimensional thermoelectric structures. We presented a novel use for a recently developed silica host. Semiconductors of thermoelectric interest, including arsenic, were deposited rather easily in these structures.

Future Directions

Although much knowledge was gained from these experiments, further research is warranted. The alloys produced in chapter 5 were not optimally doped. A route to the pressure tuned $Sb_{1.5}Bi_{0.5}Te_3$ could also be found using As_2Te_3 along with Sb_2Se_3. Such experiments might further tune known good room temperature thermoelectrics.

The research contained in chapter 6 though, has much room for exciting new research. Using a very young technique, we showed the simplicity of depositing semiconductors in these porous silica hosts. Experiments are already underway to demonstrate deposition of materials with and without a hydride precursor. Methods being experimented with include the vapor-liquid-solid method and the vapor-phase deposition method used in other thermoelectric experiments[38, 104]. This field is moving rapidly and techniques are being tested and refined daily.

References

[1] G. B. Abdullaev, A. A. Bashshaliev, and S. A. Aliev. The heat conductivity of solid solutions of Sb_2S_3 and Se_2Se_3. *Russian Physics: Rep. Nat. Acad. of Sci. of Azerbaijan*, 17:877–879, 1961.

[2] D. Adler. *Amorphous Semiconductors*. CRC Press, Cleveland, 1971.

[3] C. Ambrosch-Draxl and J. O. Sofo. Linear optical properties of solids within the full-potential linearized augmented planewave method. Los Alamos National Laboratory, Preprint Archive, Condensed Matter, 2004.

[4] N. W. Ashcroft and N. D. Mermin. *Solid State Physics*. Saunders College, 1976.

[5] T. Atou and J. V. Badding. A high resolution laboratory-based high pressure x-ray diffraction system. *Rev. Sci. Inst.*, 66:4496–4500, 1995.

[6] I. G. Austin and A. Sheard. Optical properties of Bi_2Te_3-Bi_2Se_3 alloys. *J. Electronics and Control*, 3:236–237, 1957.

[7] J. V. Badding, J. F. Meng, and D. A. Polvani. Pressure tuning in the search for new and improved solid state materials. *Chem. Mater.*, 10:2889–2894, 1998.

[8] S. G. Bishop and N. J. Shevchik. Densities of valence states of amorphous and crystalline As_2S_3, As_2Se_3, and As_2Te_3. *Phys. Rev. B*, 12:1567–1578, 1975.

[9] M. T. Björk, B. J. Ohlsson, T. Sass, A. I. Persson, C. Thelander, M. H. Magnusson, K. Deppert, L. R. Wallenberg, and L. Samuelson. One-dimensional steeplechase for electrons realized. *Nano Lett.*, 2:87–89, 2002.

[10] J. Black, E. M. Conwell, L. Seigle, and C. W. Spencer. Elecrical and optical properties of some $M_2^{V-B}N_3^{VI-B}$ semiconductors. *J. Phys. Chem. Solids*, 2:240–251, 1957.

[11] P. Blaha, K. Schwarz, G. K. H. Madsen, D. Kvasnicka, and J. Luitz. *WIEN2k: An Augmented Plane Wave + Local Orbitals Program for Calculating Crystal Properties.* Techn. Universitat Wien, Austria, Karlheinz Schwarz, 2001.

[12] P. E. Blochl, O. Jepsen, and O. K. Andersen. Improved tetrahedron method for brillouin-zone integrations. *Phys. Rev. B*, 49:16223, 1994.

[13] D. A. Broido and T. L. Reinecke. Thermoelectric transport in quantum well and quantum wire supperlattices. In R. K. Willardson and A. C. Beer, editors, *Semiconductors and Semimetals*, volume 71, pages 123–155. Academic Press, 2001.

[14] D. W. Bullett. Electronic structure of arsenic chalcogenides. *Phys. Rev. B*, 14:1683–1692, 1976.

[15] F. P. Bundy. Effect of pressure on emf of thermocouples. In F. P. Bundy, W. R. Hibbard Jr., and H. M. Strong, editors, *Progress in very high pressure research*, pages 256–265, 1961.

[16] G. J. Carron. The crystal structure and powde data for arsenic telluride. *Acta Cryst.*, 16:338–343, 1962.

[17] A.-B. Chen and A. Sher. *Semiconductor Alloys: Physics and Materials Engineering.* Plenum Press, 1995.

[18] I. Chen. Molecular orbital studies of As_2S_3, and As_2Se_3. *Phys. Rev. B*, 8:1440–1444, 1973.

[19] J. Cornet and D. Rossier. Properties and structure of As-Te glasses (II): local order parameters and structural model. *J. Non-Cryst. Solids*, 12:85–99, 1973.

[20] R. T. Delves, A. E. Bowley, D. W. Hazelden, and H. J. Goldsmid. Anisotropy of the electrical conductivity in Bi_2Te_3. In *Proc. Phys. Soc. London*, volume 78, page 838, 1961.

[21] F. J. DiSalvo. Thermoelectric cooling and power generation. *Science*, 285:703–706, 1999.

[22] J. R. Drabble, R. Groves, and R. Wolfe. Galvanomagnetic effects in n-type bismuth telluride. In *Proc. Phys. Soc. London*, volume 71, pages 430–443, 1958.

[23] M. S. Dresselhaus, G. Dresselhaus, X. Sun, Z. Zhang, S. B. Cronin, and T. Koga. Low-dimensional thermoelectric materials. In *Physics of the Solid State*, volume 41, pages 679–682, 1999.

[24] M. S. Dresselhaus, Y.-M. Lin, M. R. Black, O. Rabin, and G. Dresselhaus. New directions for low dimensional thermoelectricity. In *Mater. Res. Soc. Symp. Proc.*, volume 793, pages 419–430, 2004.

[25] M. S. Dresselhaus, Y.-M. Lin, S. B. Cronin, O. Rabin, M. R. Black, and G. Dresselhaus. Quantum wells and quantum wires for potential thermoelectric applications. In R. K. Willardson and A. C. Beer, editors, *Semiconductors and Semimetals*, volume 71, pages 1–121. Academic Press, 2001. Recent Trends in Thermoelectric Materials Research III.

[26] M. S. Dresselhaus, Y.-M. Lin, O. Rabin, M. R. Black, S. B. Cronin, and G. Dresselhaus. Overview of bismuth nanowires for thermoelectric applications. In *Chemistry, Physics, and Materials Science of Thermoelectric Materials: Beyond Bismuth Telluride*, pages 1–17, 2003.

[27] M. S. Dresselhaus, Y.-M. Lin, O. Rabin, and G. Dresselhaus. bismuth nanowires for thermoelectric applications. *Microscale Thermophysical Engineering*, 7:207–219, 2003.

[28] J. T. Edmond. Electronic conductivity in As_2Se_3, As_2Se_2Te and similar materials. *Br. J. Appl. Phys.*, 17:979–989, 1966.

[29] M. H. Ettenberg, J. R. Maddux, P. J. Taylor, W. A. Jesser, and F. D. Rosi. Improving yield and performance in pseudo-ternary thermoelectric alloys $(Bi_2Te_3)(Sb_2Te_3)(Sb_2Se_3)$. *J. Cryst. Growth*, 179:495–502, 1997.

[30] R. A. Forman, G. J. Piermarini, J. D. Barnett, and S. Block. Pressure measurement made by the utilization of ruby sharp-line luminescence. *Science*, 176:284–285, 1972.

[31] L. Friedman. Thermopower of superlattices as a probe of the density of states distribution. *J. Phys. C: Sol. St. Phys.*, 17(22):3999–4008, 1984.

[32] H. J. Goldsmid. title. In *Proc. Phys. Soc. London Sect. B*, volume 69, page 203, 1956.

[33] H. J. Goldsmid. *Thermoelectric Refrigeration*. Plenum Press, 1964.

[34] E. K. U. Gross, C. A. Ullrich, and U. J. Gossman. Density functional theory of time-dependent systems. In E. K. U. Gross and R. M. Dreizler, editors, *Density Functional Theory*, volume 337 of NATO ASI Series B, page 149. Plenum Press, 1995.

[35] M. S. Gudiksen, J. Wang L. J. Lauhon, D. C. Smith, and C. M. Lieber. Growth of nanowire superlattice structures for nanoscale photonics and electronics. *Nature*, 415:617–620, 2002.

[36] T. C. Harman, B. Paris, S. E. Miller, and H. L. Goering. Preparation and some physical properties of Bi_2Te_3, Sb_2Te_3 and As_2Te_3. *J. Phys. Chem. Solids*, 26:181–190, 1957.

[37] T. C. Harman, P. J. Taylor, M. P. Walsh, and B. E. LaForge. Quantum dot superlattice thermoelectric materials and devices. *Science*, 297:2229–2232, 2002.

[38] J. Heremans, C. M. Thrush, Y.-M. Lin, S. B. Cronin, Z. Zhang, M. S. Dressel-haus, and J. F. Mansfield. Bismuth nanowire arrays: Synthesis and galvomagnetic properties. *Phys. Rev. B*, 61:2921–2930, 2000.

[39] J. P. Heremans. Thermoelectric transport in bismuth nanowires: Experimental results. In *Chemistry, Physics, and Materials Science of Thermoelectric Materials: Beyond Bismuth Telluride*, pages 185–201, 2003.

[40] J. P. Heremans. Thermoelectric power, electrical and thermal resistance, and mag-netoresistance of nanowire composites. In *Mater. Res. Soc. Symp. Proc.*, volume 793, pages 3–14, 2004.

[41] L. D. Hicks and M. S. Dresselhaus. Effect of quantum-well structures on the thermoelectric figure of merit. *Phys. Rev. B*, 47:12727–12731, 1993.

[42] L. D. Hicks and M. S. Dresselhaus. Thermoelectric figure of merit of a one-dimensional conductor. *Phys. Rev. B*, 47:16631–16634, 1993.

[43] P. Hohenberg and W. Kohn. Inhomogeneous electron gas. *Phys. Rev.*, 136:B864, 1964.

[44] K. Inoue, M. Wada, K. Sakoda, A. Yamanaka, M. Hayashi, and J. W. Haus. Fabrication of two-dimensional photonic band structure with near-infrared band gap. *Jap. J. Appl. Phys.*, 33:L1463–L1465, 1994.

[45] J.-P. Issi J. Heremans, A. A. M. Rashid, and G. A. Saunders. Electrical and thermal transport properties of arsenic. *J. Phys. C: Sol. St. Phys.*, 10:4511–4522, 1977.

[46] A. S. Kanishcheva, Y. N. Milhailov, and A. P. Chernov. Refinement of the crystal structure of arsenic telluride. *Izvestiya Akademii Nauk SSSR Neorg. Mat.*, 18:949–952, 1982.

[47] B. A. Khan, P. Bai, and D. Adler. Electronic structure of amorphous arsenic telluride. *J. Non-Cryst. Solids*, 66:321–326, 1984.

[48] L. G. Khvostantsev, A. I. Orlov, N. K. Abrikosov, and L. D. Ivanova. Thermo-electric properties and phase transition in antimony telluride under hydrostatic pressure up to 9 *GPa*. *Phys. Status Solidi A: App. Res.*, 58:37–40, 1980.

[49] V. A. Kirkinskii and V. G. Yakushev. Arsenic-Tellurium system at high pressures. *Neorg. Mat.*, 10(8):1431–1435, 1974.

[50] J. C. Knight, T. A. Birks, B. J. Mangan, and P. St. J. Russell. Microstructured silica an an optical-fiber material. *MRS Bull.*, 26:614–617, 2001.

[51] J. C. Knight, T. A. Birks, P. St. J. Russell, and D. M. Atkin. All-silica single-mode optical fiber with photonic crystal cladding. *Opt. Lett.*, 21:1547–1549, 1996.

[52] T. Koga, S. B. Cronin, M. S. Dresselhaus, J. L. Liu, and K. L. Wang. Experimental proof-of-principle investigation of enhanced $Z_{3D}T$ in (001) oriented Si/Ge superlattices. *Appl. Phys. Lett.*, 77:1490–1492, 2000.

[53] W. Kohn and L. J. Sham. Self-consistent equations including exchange and correlation effects. *Phys. Rev.*, 140:A1133, 1965.

[54] F. Kosek, J. Tulka, and L. Stourac. title. *Czech. J. Phys.*, 28:page 325, 1978.

[55] J. S. Lannin, J. M. Calleja, and M. Cardona. Second-order raman scattering in the group-V_b semimetals: Bi, Sb, and As. *Phys. Rev. B*, 12:585–593, 1975.

[56] P. Larson, S. D. Mahanti, and M. G. Kanatzidis. Electronic structure and transport of Bi_2Te_3 and $BaBiTe_3$. *Phys. Rev. B*, 61:8162, 2000.

[57] Y.-M. Lin, O. Rabin, S. B. Cronin, J. Y. Ying, and M. S. Dresselhaus. Semimetal-semiconductor transition in $Bi_{1-x}Sb_x$ alloy nanowires and their thermoelectric properties. *Appl. Phys. Lett.*, 81:2403–2405, 2002.

[58] P. E. Lippens, E. Brousse, J. Olivier-Fourcade, A. Gheorghiu de la Rocque, and C. Sénémaud. Electronic structure of As_2Te_3-GeTe crystalline compounds. *J. Phys. Chem. Solids*, 62:467–474, 2001.

[59] O. Madelung. *Introduction to Solid-State Theory.* Springer-Verlag, 1978.

[60] G. K. H. Madsen. Private communication.

[61] G. D. Mahan. Good thermoelectrics. In H. Ehrenreich and F. Spaepen, editors, *Solid State Physics*, volume vol. 51, pages 81–156. Academic Press, 1998.

[62] G. D. Mahan and J. O. Sofo. The best thermoelectrics. In *Proc. Natl. Acad. Sci. USA*, volume 65, page 7436, 1996.

[63] R. B. Mallison, J. A. Rayne, and R. W. Ure Jr. de haas-van alphen effect in n-type Bi_2Te_3. *Phys. Rev.*, 175:1049–1056, 1968.

[64] M. A. McGuire. Private communication.

[65] S. K. Mishra, S. Satpathy, and O. Jepsen. Electronic structure and thermoelectric properties of bismuth telluride and bismuth selenide. *J. Phys.: Condens. Matter*, 9:461, 1997.

[66] B. R. Nag. *Electron Transport in Compound Semiconductors.* Springer Verlag, 1980.

[67] J. Nagao, M. Ferhat, E. Hatta, and K. Mukasa. Anisotropic factor of electrical conductivity in p-Bi_2Te_3 crystals. *Phys. Stat. Sol. B*, 219:347, 2000.

[68] S. Nakajima. The crystal structure of $Bi_2Te_{3-x}Se_x$. *J. Phys. Chem. Solids*, 24:479, 1963.

[69] J. H. Nguyen and R. Jeanloz. A computer program to analyze x-ray diffraction films. *Rev. Sci. Instrum.*, 64:3456–3461, 1993.

[70] J. P. Perdew, K. Burke, and M. Ernzerhof. Generalized gradient approximation made simple. *Phys. Rev. Lett.*, 77:3865, 1996.

[71] N. S. Platakis. Phase transitions and electrical properties of As_2Te_3. *J. Non-Cryst. Solids*, 24:365–376, 1977.

[72] D. A. Polvani, J. F. Meng, M. Hasegawa, and J. V. Badding. Measurement of the thermoelecric power of very small samples at ambient and high pressures. *Rev. Sci. Instrum.*, 70:3586–3589, 1999.

[73] D. A. Polvani, J. F. Meng, N. V. C. Shekar, J. Sharp, and J. V. Badding. Large improvement in thermoelectric properties in pressure-tuned p-type $Sb_{1.5}Bi_{0.5}Te_3$. *Chem. Mater.*, 13:2068–2071, 2001.

[74] O. Rabin, G. Chen, and M. S. Dresselhaus. Crystallographically-oriented electrochemically-deposited bismuth nanowires. In *Mater. Res. Soc. Symp. Proc.*, volume 793, pages 127–132, 2004.

[75] J. B. Renucci, W. Richter, M. Cardona, and E. Schoenherr. Resonance raman scattering in group V_b semimetals: arsenic, antimony, and bismuth. *Phys. Status Solidi B: Basic Res.*, 60:299–308, 1973.

[76] D. L. Rode. Low-field electron transport. In R. K. Willardson and A. C. Beer, editors, *Semiconductors and Semimetals*, volume 10, pages 1–89. Academic Press, 1975. Transport Phenomena.

[77] J. Rodriguez-Carvajal. Fullprof: A program for rietveld refinement and pattern matching analysis. In *Abstracts of the Satellite Meeting on Powder Diffraction of the XV Congress of the IUCr*, page 127. Toulouse, France, 1990.

[78] B. Rönnlund, O. Beckman, and H. Levy. Doping properties of Sb_2Te_3 indicating a two valence band model. *J. Phys. Chem. Solids*, 26:1281–1286, 1965.

[79] A. Rosenberg, T. J. Tonucci, H.-B. Lin, and A. J. Campillo. Near-infrared two-dimensional photonic band-gap materials. *Opt. Lett.*, 21:830–832, 1996.

[80] N. Sakai, T. Kajiwara, K. Takemura, S. Minomura, and Y. Fujii. Pressure-induced phase transition in Sb_2Te_3. *Solid State Comm.*, 40:1045–1047, 1981.

[81] D. E. Sands. *Introduction to Crystallography.* Dover, 1993.

[82] P. Sazio. Private communication.

[83] P. Sazio, T. J. Scheidemantel, and J. V. Badding. Semiconductor-filled holey fibers as waveguides. In Preparation.

[84] T. J. Scheidemantel, C. Ambrosch-Draxl, T. Thonhauser, J. V. Badding, and J. O. Sofo. Transport coefficients from first-priniciples calculations. *Phys. Rev. B*, 68:125210, 2003.

[85] T. J. Scheidemantel and J. V. Badding. Electronic structure of $\beta-\text{As}_2\text{Te}_3$. *Solid State Comm.*, 127:667–670, 2003.

[86] R. Sehr and L. R. Testardi. The optical properties of p-type $\text{Bi}_2\text{Te}_3\text{–Sb}_2\text{Te}_3$ alloys between 2–15 microns. *J. Phys. Chem. Solids*, 23:1219, 1962.

[87] A. K. Singh and Geetha Ramani. Measurement of thermoelectric power of solids up to 10 GPa. *Rev. Sci. Instrum.*, 49(9):1324–1326, 1978.

[88] G. A. Slack. *CRC Handbook of Thermoelectrics.* CRC Press, 1995.

[89] J. O. Sofo and G. D. Mahan. Optimum band gap of a thermoelectric material. *Phys. Rev. B*, 49:4565–4570, 1994.

[90] J. O. Sofo, G. D. Mahan, and J. Barrs. Transport coefficients and thermoelectric figure of merit of n-$Hg_{1-x}Cd_xTe$. *J. Appl. Phys.*, 76:2249, 1994.

[91] V. V. Sologub, A. D. Goletskaya, and R. V. Parfen'ev. Bismuth sesquitelluride valence band. *Fiz. Tverd. Tela (Leningrad) [Sov. Phys. Solid State]*, 14:914–917, 1972.

[92] H. Sthioul, D. Jaccard, and J. Sierro. Thermoelectric power of cerium-palladium $(CePd_{3+\varepsilon})$, cerium-palladium-rhodium $(Ce(Pd_{1-x}Rh_x)_3)$ and cerium-palladium-silver $(Ce(Pd_{1-y}Ag_y)_3)$. In P. Wachter and H. Boppart, editors, *Proc. Int. Conf.:Valence Instabilities*, pages 443–455, 1982.

[93] H. E. Swanson and E. Tatge. Standard x-ray diffraction patterns. *National Bureau of Standards Circular*, 1953.

[94] Z. Tao and L. Friedman. Thermoelectric power of superlattices. ii. *J. Phys. C:Sol. St. Phys.*, 18(16):L455–L461, 1985.

[95] I. Teramoto and S. Takayanagi. Relations between the electronic properties and the chemical bonding of $Sb_xBi_{2-x}Te_{3-y}Se_y$ system. *J. Phys. Chem. Solids*, 19:124–129, 1961.

[96] T. Thonhauser, T. J. Scheidemantel, and J. O. Sofo. Improved thermoelectric properties in bismuth alloys. Accepted for Publication.

[97] T. Thonhauser, T. J. Scheidemantel, J. O. Sofo, J. V. Badding, and G. D. Mahan. Thermoelectric properties of Sb_2Te_3 under pressure and uniaxial stress. *Phys. Rev. B*, 68:085201, 2003.

[98] R. J. Tonucci, B. L. Justus, A. J. Campillo, and C. E. Ford. Nanochannel array glass. *Science*, 258:783–785, 1992.

[99] S. Toscani, J. Dugue, R. Ollitrault, and R. Ceolin. Polymorphism of arsenic sesquitelluride: structural studies and thermal behavior of rhombohedral $\beta-As_2Te_3$. *Thermochim. Acta*, 186(2):247–251, 1991.

[100] C. Uher. Structure-property relations in skutterudites. In *Chemistry, Physics, and Materials Science of Thermoelectric Materials: Beyond Bismuth Telluride*, pages 121–146, 2003.

[101] R. Venkatasubramanian, B. O'Quinn, E. Siivola, K. Coonley, P. Addepally, M. Napier, and T. Colpitts. Superlattice thin-film thermoelectric materials and devices. In *Mater. Res. Soc. Symp. Proc.*, volume 793, pages 51–58, 2004.

[102] R. Venkatasubramanian, E. Siivola, T. Colpitts, and B. O'Quinn. Thin-film thermoelectric devices with high room-temperature figures of merit. *Nature*, 413:597–602, 2001.

[103] C. B. Vining. A model for the high-temperature transport properties of heavily doped n-type silicon-germanium alloys. *J. Appl. Phys.*, 69:331, 1991.

[104] R. S. Wagner and W. C. Ellis. Vapor-liquid-solid mechanism of single crystal growth. *Appl. Phys. Lett.*, 4:89–90, 1964.

[105] Y. Wu, R. Fan, and P. Yang. Block-by-block growth of single-crystalline Si/SiGe superlattice nanowires. *Nano Lett.*, 2:83–86, 2002.

[106] J. Yang. Thermal conduction in $CoSb_3$-based skutterudites. In *Chemistry, Physics, and Materials Science of Thermoelectric Materials: Beyond Bismuth Telluride*, pages 169–184, 2003.

[107] R. Yang and G. Chen. Theoretical thermal conductivity of periodic two-dimensional nanocomposites. In *Mater. Res. Soc. Symp. Proc.*, volume 793, pages 121–126, 2004.

[108] E. I. Yarembash and E. S. Vigileva. Reaction between bismuth and arsenic tellurides. *Russian Journal of Inorganic Chemistry*, 7:1437–1440, 1962.

[109] W. M. Yim and F. D. Rosi. Comound tellurides and their alloys for peltier cooling - a review. *Solid-State Electronics*, 15:1121–1140, 1972.

[110] S. J. Youn and A. J. Freeman. First-principles electronic structure and its relation to thermoelectric properties of Bi_2Te_3. *Phys. Rev. B*, 63:085112, 2001.

[111] J. M. Ziman. *Principles of the Theory of Solids.* Cambridge University Press, 1972.

Vita

Thomas J. Scheidemantel was born in New Brighton, Pennsylvania on June 9, 1971. He is the only son of Thomas G. and Margaret A. Scheidemantel and the only sibling of Beth A. Scheidemantel. He was raised in Beaver Falls, Pennsylvania where he attended Blackhawk High School. He then served in the United State Coast Guard after which he received a Bachelor of Science degree in Physics from The Pennsylvania State University. After graduation in 1998, he remained in University Park and began graduate work in the physics department, and joined the research group of Professor John Badding in the chemistry department. Upon completion of his Ph.D. in the summer of 2004, he accepted a post-doctoral position, also at The Pennsylvania State University, working on granular materials under the direction of Professor Peter E. Schiffer.